J. Fluid Mech. (2024), *vol*. 980, A51, doi:10.1017/jfm.2024.53

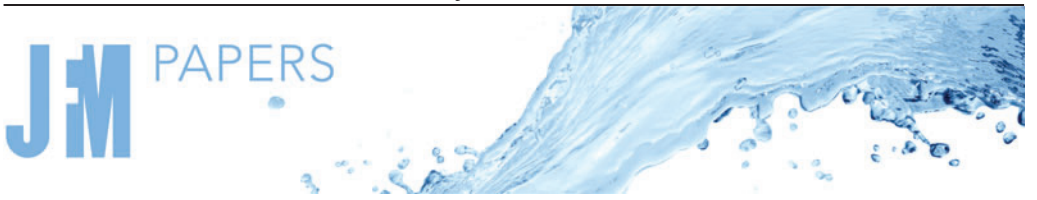

Direct numerical simulations of turbulent channel flow with a rib-roughened porous wall

Kazuhiko Suga[1],† **and Yusuke Kuwata**[1]

[1]Department of Mechanical Engineering, Osaka Metropolitan University, Osaka 599-8531, Japan

(Received 1 March 2023; revised 9 December 2023; accepted 8 January 2024)

To describe the effects of porous roughness on turbulence, we have carried out direct numerical simulations using the lattice Boltzmann method. The simulated flows are fully developed turbulent flows in channels consisting of a solid smooth top wall and a porous bottom wall with transverse porous ribs whose heights are 10 % of the channel height. The considered ratios of the rib spacing to the rib height are $w/k \simeq 1$ and 9. The Kelvin-cell structure is applied to construct faithfully the porous media whose porosities are $\varphi \geq 0.79$. Three kinds of porous media having different permeabilities are considered. The most permeable one has an approximately one order higher permeability than that of the least permeable one. The higher permeability case is designed to have a pore scale that is the same as the rib height so that it is the most permeable case for the rib roughness with the designed porosity. In the simulations, the bulk Reynolds number is set to $Re_b = 5500$, and the corresponding permeability Reynolds numbers are $Re_K = 2.2$–7.5. The simulated field data and the drag coefficient, which includes both the pressure drag by the ribs and the frictional drag over the porous wall, are analysed to understand the characteristics of the permeable roughness in terms of permeability. The decomposition of the drag coefficient into the integrated laminar, rib-drag, dispersion and turbulence parts elucidates the transition mechanism between the typical d-type to k-type roughness depending on Re_K. By the double (time and space) averaged budget equations for the dispersion and Reynolds stresses, we explain how the energy generated by the roughness transfers to turbulence through dispersion resulting in the k-type characteristics. The nominal roughness sublayer thickness and the characteristic roughness height are introduced with the parameters obtained by fitting the velocity data to Best's and Nikuradse's logarithmic velocity formulae. Along with data in the literature, it is suggested that the ratio of the characteristic roughness height to the nominal roughness sublayer thickness becomes constant irrespective of the rib spacing in the full permeable-wall turbulence at $Re_K > 7$.

Key words: turbulence simulation, porous media, channel flow

† Email address for correspondence: suga@omu.ac.jp

1. Introduction

Since wall roughness is a common issue in engineering fluid flows, the effects of rough walls on turbulence have been studied by many researchers, as seen in review articles by Raupach, Antonia & Rajagopalan (1991), Jiménez (2004), Piomelli (2019) and Chung *et al.* (2021). The rough wall turbulence has been described often by the roughness function that depends on a representative scale, and Perry, Schofield & Joubert (1969) suggested that such roughness characteristics could be categorized into two types: k- and d-types. For the k-type roughness, the representative scale is the roughness scale, while for the d-type roughness, it is the boundary layer thickness or the pipe diameter. According to Tani (1987), for regularly spaced rib roughness, usually it has been considered that the demarcating ratio of the rib spacing w to the rib height k is $w/k = 3$, and the k-type roughness is at $w/k > 3$, while the d-type roughness is at $w/k < 3$. Note that recent studies such as MacDonald *et al.* (2018) and Xu *et al.* (2021), however, showed that non-k-type roughness was not automatically classified as d-type roughness. Also, the direct numerical simulations (DNS) by Lee & Sung (2007) pointed out that there was strong turbulence interaction between inner and outer layers induced by the surface roughness. Hence the categorization may not be that simple. Anyway, in the so-called k-type rough wall turbulence, as seen in Cui, Patel & Lin (2003), Leonardi *et al.* (2003) and Ashrafian, Andersson & Manhart (2004), there are recirculation bubbles that reattach ahead of the next ribs, hence the ribs are exposed to outflows. It was also reported that the roughness function became maximum at approximately $w/k = 7$ (Flack & Schultz 2014). In fact, by performing DNS, Leonardi *et al.* (2003) reported that the roughness function increased monotonically up to $w/k \simeq 7$ and then maintained the level though very gradually decreased as w/k increased. In the conventional d-type roughness at $w/k < 3$, there are stable recirculation bubbles between the ribs, and they are isolated from outflows (Cui *et al.* 2003; Leonardi *et al.* 2003, 2004).

As mentioned above, a significant amount of understanding of turbulence over rib-roughened surfaces has been accumulated. We, however, emphasize that the roughness elements discussed so far have been usually impermeable, but the roughness elements are sometimes recognized to be permeable, particularly in the river bed flows (e.g. Padhi *et al.* 2018; Shen, Yuan & Phanikumar 2020). Some metal–foam heat exchangers also have ribbed or finned surfaces (Feng *et al.* 2018; Wang *et al.* 2020). It is hence required to understand the effects of permeable rough surfaces on turbulence. The wall permeability usually increases near-wall turbulence (e.g. Lovera & Kennedy 1969; Zippe & Graf 1983; Manes *et al.* 2009; Pokrajac & Manes 2009; Suga *et al.* 2010), and many studies including ours (Breugem, Boersma & Uittenbogaard 2006; Manes, Poggi & Ridol 2011; Suga 2016; Suga, Nakagawa & Kaneda 2017; Manes *et al.* 2011; Voermans, Ghisalberti & Ivey 2017) applied the permeability Reynolds number as a measure to characterize turbulence over porous media. Here, the permeability Reynolds number is based on the square root of the permeability K and the friction velocity. It is true particularly for isotropic porous media, although Rosti, Brandt & Pinelli (2018) and Gómez-de Segura & García-Mayoral (2019) reported numerical studies that indicated turbulent drag reduction over anisotropic porous media with high streamwise permeabilities. By particle image velocimetry (PIV) experiments for turbulence in a block-mounted channel, Suga *et al.* (2013) showed that the turbulence level over a porous square-cylinder block was lower than that over an impermeable block. We thus expect that permeable roughness increases turbulence, though its level may not exceed that over impermeable roughness. In this study, roughness with permeability is termed 'permeable roughness'.

In the recent literature, there have been several studies for permeable roughness. Kim, Blois & Christensen (2020) measured the dynamic interplay between surface and subsurface flows over rough permeable beds consisting of cubically packed spheres. Their observation indicated that the presence of bed roughness intensified the strength of flow penetration by large-scale near-surface flow structures. Since the large-scale flow structure enhances dispersion velocities, it is considered that dispersion played an important role in their results. As for numerical studies, Shen *et al.* (2020) discussed flows over sediments with rough surfaces by DNS. They reported that turbulence was affected significantly by the roughness, resulting in the modification of the penetration depth and hence the mass flux across the interface. They pointed out that the enhanced wall-normal dispersion velocity played a significant role in the enhancement of the wall-normal mixing. Stoyanova *et al.* (2019) simulated to investigate turbulent drag by permeable roughness. Their results showed that an isotropic roughness structure increased the drag more than an anisotropic structure. Since isotropic roughness structures increase dispersion velocities more, it is considered that their drag increase was partly dependent on the dispersion. To the best of the authors' knowledge, however, except for the experimental studies by the authors' group (Okazaki *et al.* 2020, 2021, 2022), there has been no study that reports systematically turbulence over rib-roughened porous walls in the literature, so far.

To understand the permeable roughness effect, Okazaki *et al.* (2022) summarized the PIV measurements carried out systematically for turbulent flows over rib-roughened porous walls. The cases were for regularly aligned square ribs whose spacings were $w/k = 1$–19, which correspond to the condition from the d-type to k-type roughness of Perry *et al.* (1969) for impermeable cases. Their experiments confirmed that since the flow rate through the ribs increased as the permeability increased, the recirculation bubbles between the ribs shifted downstream and to the bottom wall. This change of the flow patterns at $w/k < 3$ enhanced turbulence around the rib-top region. At $w/k = 1$, because the permeability enhanced the transition from the d-type to k-type characteristics, the magnitude of turbulence became larger depending on the permeability. At $w/k > 3$, the increase of turbulence by the permeability became unclear since the transition to the k-type was completed. At $w/k \geq 7$, since the permeability reduced the pressure drag of the rib roughness, the turbulence level reduced slightly as the permeability increased. These trends were reflected in the profiles of drag and the equivalent sand grain roughness height. The permeability also enhanced the transition to the 'nominally fully rough' regime. It is, however, unknown what mechanisms are working behind the above observed trends. Also, there is no knowledge of the relation between the characteristic scales of turbulence modified by the permeable roughness.

Therefore, this study discusses the effects of the permeable rib roughness on turbulence and its structure by performing DNS. We apply the multiple-relaxation-time lattice Boltzmann method (MRT LBM) (d'Humières *et al.* 2002; Suga *et al.* 2015) to the simulation scheme. The considered flow geometry is a plane channel with a porous rib-roughened bottom wall. The bottom wall and the square ribs are made of the same porous media consisting of Kelvin cell foam structures (Thomson 1887). Three permeability (low, medium and high) cases are considered to construct the porous media. We focus on $w/k = 1$ and 9 cases since they are representatives of d- and k-type roughness in impermeable cases. For all flow cases, the bulk Reynolds number $Re_b = U_b H/\nu$ is set at $Re_b = 5500$ where H, ν and U_b are the channel height, the kinematic fluid viscosity and the bulk mean velocity for the flow region above the rib-bottom.

2. Numerical procedure

In the LBM, which is based on the regular lattice configuration, the bounce-back treatment for fluid–solid boundaries is very simple, and the linear interpolated bounce-back scheme of Pan, Luo & Miller (2006) has the second-order accuracy to reproduce curved shapes (Chun & Ladd 2007). Since the LBM calculates temporal terms explicitly, and does not require solving the Poisson equation for the pressure field, we recognize its great advantage in parallel computations for flow fields resolved by hundreds of millions of lattice node points using general-purpose graphics processing units. Its accuracy is second order in time and space (Holdych *et al.* 2004). Accordingly, many studies including ours (e.g. Chukwudozie & Tyagi 2013; Fattahi *et al.* 2016; Kuwata & Suga 2017) applied the LBM successfully to porous medium flows. The present study hence applies the LBM to simulate turbulence fields, including microscopically reproduced porous medium regions with fidelity. The presently applied three-dimensional version employs 27 discrete velocities and the multiple relaxation time for the streaming velocities and the collision operator, respectively. It is hence called the D3Q27 MRT LBM (Suga *et al.* 2015).

In the D3Q27 MRT LBM, the time evolution equation of the distribution function f_α ($\alpha = 0$–26) can be written as

$$\left|f(\boldsymbol{x} + \boldsymbol{\xi}_\alpha\, \delta t, t + \delta t)\right\rangle - |f(\boldsymbol{x}, t)\rangle = -\boldsymbol{M}^{-1}\hat{\boldsymbol{S}}\left(|m(\boldsymbol{x}, t)\rangle - \left|m^{eq}(\boldsymbol{x}, t)\right\rangle\right), \tag{2.1}$$

where the notation such as $|f\rangle$ means $|f\rangle = {}^{\mathrm{T}}(f_0, f_1, \ldots, f_{26})$, $\boldsymbol{x}$ is the position vector, $\boldsymbol{\xi}_\alpha$ is the discrete velocity, and δt is the time step. The matrix $\boldsymbol{M}$ is a 27×27 matrix that linearly transforms the distribution functions to the moments as $|m\rangle = \boldsymbol{M}\,|f\rangle$. The collision matrix $\hat{\boldsymbol{S}}$ is diagonal, and the equilibrium moment is $|m^{eq}\rangle = \boldsymbol{M}\,|f^{eq}\rangle$. The local equilibrium distribution function is

$$f_\alpha^{eq} = w_\alpha \left\{\rho + \rho_0 \left(\frac{\boldsymbol{\xi}_\alpha \cdot \boldsymbol{u}}{c_s^2} + \frac{(\boldsymbol{\xi}_\alpha \cdot \boldsymbol{u})^{\,2} - c_s^2\,|\boldsymbol{u}|^2}{2c_s^4}\right)\right\}, \tag{2.2}$$

where w_α is the weighting coefficient, c_s is the sound speed in the LBM, $\boldsymbol{u}$ is the fluid velocity, and ρ is the fluid density that is expressed as the summation of constant and fluctuation parts, $\rho = \rho_0 + \delta\rho$ (He & Luo 1997). The macroscopic fluid variables such as the density, momentum and pressure are calculated by $\rho = \sum_\alpha f_\alpha$, $\rho_0 u_i = \sum_\alpha \boldsymbol{\xi}_{\alpha i} f_\alpha$ and $p = c_s^2 \rho$, respectively. See Appendix A for the detailed parameters, coefficients and matrices. Since we apply local mesh refinement to the porous region, the imbalance correction grid-refinement method by Kuwata & Suga (2016*a*) is used.

3. Computational conditions

3.1. *Porous structure and computational domain*

The considered porous media consist of the Kelvin cells (or tetrakaidecahedrons). The Kelvin cell is a polyhedron shape that has been studied in conjunction with foams and the minimal surface area. It had been thought the best model for the space-filling shape with minimal surface area until the study of Weaire & Phelan (1994), and has been often applied as a model for regular, monodisperse 'foam'. Since one of the aims of this study is to understand the flows over rib-roughened foam beds measured by our group (Okazaki *et al.* 2022), we choose the Kelvin cells to model the foam structure applied in the experiments.

Indeed, Kelvin cells have been applied in several studies on porous medium flows, as reviewed by Kumar & Topin (2017). To form the open cell structures, we apply circular

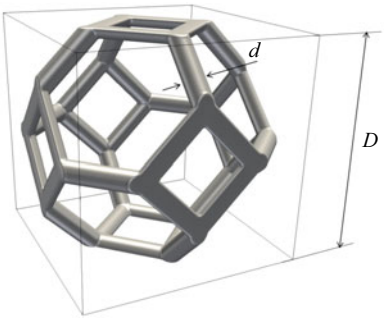

Figure 1. Unit cell of the Kelvin cell.

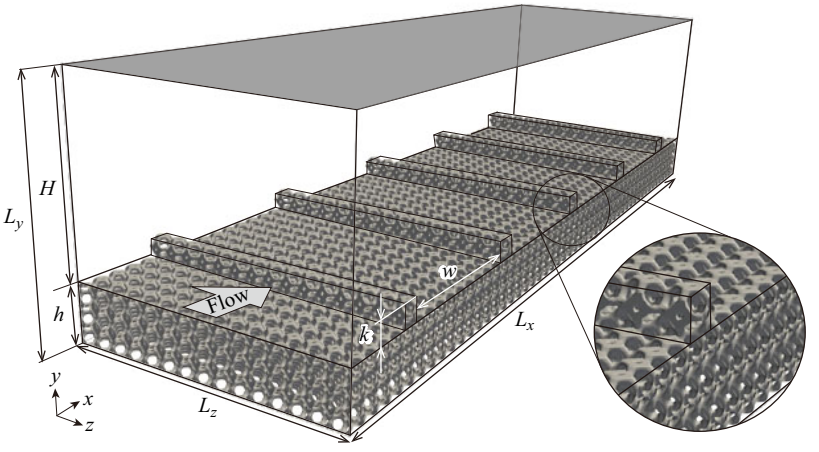

Figure 2. Computational domain; the streamwise, wall-normal and spanwise directions are denoted as x-, y- and z-directions.

cross-sectioned ligaments as illustrated in figure 1, where D and d are the unit cell height and the ligament diameter, respectively. In the present study, $D/d = 5$ and 8.25 make porosity $\varphi = 0.79$ and 0.91, respectively.

Figure 2 illustrates the computational domain. The channel height H is the distance between the upper wall and the surface of the porous layer. The upper wall and the very bottom of the porous layer are treated as smooth no-slip surfaces, although a symmetrical configuration is useful to obtain the drag because it balances with the pressure drop. On the other hand, in the present configuration, we can obtain the drag by the ribbed surface by subtracting the top smooth wall friction from the pressure drop. Hence we can save extra computer memory for grid points to describe a porous upper wall. It should, however, certainly be considered how the presence of the upper wall turbulence affects the flow near the bottom wall. For this issue, Leonardi *et al.* (2004) compared the results of asymmetric and symmetric configurations for (solid impermeable) $w/k = 3$ with $k/H = 0.1$. Their visualizations of the two cases confirmed that the recirculation profiles between the ribs agreed well with each other. The pressure and skin friction distributions along the bottom wall also showed good agreement between the two cases. Moreover, although the maximum velocity point shifted upwards due to the roughness on the bottom wall, the normalized velocity by the wall unit showed an overlapped profile with that for

Case	w/k	k/D	φ	K/H^2 ($\times 10^{-5}$)	D/Δ^f	h/H	Box size ($L_x \times L_y \times L_z$)	Nodes ($\times 10^6$)
S1	1.0	—	—	—	40	—	$5.0H \times H \times 1.5H$	229.247
S9	9.0	—	—	—	40	—	$5.0H \times H \times 1.5H$	229.247
LP1	0.9	2	0.79	1.34	40	0.106	$5.0H \times 1.106H \times 1.5H$	1246.792
LP9	8.9	2	0.79	1.34	40	0.106	$5.0H \times 1.106H \times 1.5H$	1246.792
MP1	0.8	1	0.79	5.37	40	0.314	$5.0H \times 1.314H \times 1.5H$	373.415
MP9	8.8	1	0.79	5.37	40	0.314	$5.0H \times 1.314H \times 1.5H$	373.415
HP1	0.9	1	0.91	11.0	66	0.307	$5.0H \times 1.307H \times 1.5H$	1140.488
HP9	8.9	1	0.91	11.0	66	0.307	$5.0H \times 1.307H \times 1.5H$	1140.488

Table 1. Computational cases: HP, MP and LP are high, medium and low permeable cases, respectively, while S are solid impermeable cases. Here, k, w, φ, K and D are the rib height, rib spacing, porosity, permeability and unit height of the Kelvin cell, respectively, and Δ^f is the grid spacing for finer lattice regions.

the symmetry configuration, indicating that the roughness function was unaffected by the boundary condition on the upper wall.

For the present simulations, the rib height is also fixed at $k/H = 0.1$. From the viewpoint of Jiménez (2004), the ratio $H/k = 10$ might not be large enough, while rib-roughened turbulent channel flow studies have often applied similar roughness scales. Indeed, Hanjalić & Launder (1972) applied the ratios $H/k = 9$ and 17 for the rib-roughened channel experiments at $w/k = 9$. As for the DNS studies, Nagano, Hattori & Houra (2004) applied $H/k = 10$–40 for k- and d-type rib roughness, while Leonardi *et al.* (2003) and Orlandi, Sassun & Leonardi (2016) applied $H/k = 10$ for square and triangular rib roughness. The trends of $H/k \simeq 10$ shown in those studies, however, did not so deviate from those by large enough H/k geometries. Furthermore, the roughness sublayer thickness was suggested to be $3k$–$5k$ by Raupach *et al.* (1991), and it was less than $5k$ by the studies of Ashrafian *et al.* (2004) and Lee & Sung (2007). As discussed in Okazaki *et al.* (2022), who also applied $H/k = 10$, their ratios of the equivalent boundary layer thickness to the rib height were generally larger than six, and they showed close agreement between their impermeable results and those of Burattini *et al.* (2008), whose ratio was $H/k = 21$. Since for the rib-roughened cooling passages in turbine blades the ratios are also in such a range (e.g. Iacovides & Raisee 1999), the present discussions are useful for the practical point of view. We therefore consider that $H/k = 10$ is acceptable for discussions on rough wall turbulence, particularly for channel flow configurations.

As shown in table 1, three permeability cases: low permeable (LP), medium permeable (MP) and high permeable (HP) cases are considered for the porous media at $w/k \simeq 1$ and 9. Hereafter, cases HP1, HP9, etc. correspond to case HP at $w/k \simeq 1$, case HP at $w/k \simeq 9$, etc., respectively. (Note that the values of w/k in the present study are not integers, as explained in the next paragraph.) To calculate the permeability K, separate computations using a unit cell with a fixed pressure drop and the periodic velocity boundary condition for each direction are carried out, as seen later, in § 3.2. Using the Darcy equation, the calculated permeabilities of LP, MP and HP cases are $K/H^2 = 1.34 \times 10^{-5}$, 5.37×10^{-5} and 1.10×10^{-4}, respectively. Accordingly, the HP case is 8.2 times as permeable as the LP case. Since the experimentally applied foamed materials in Okazaki *et al.* (2022) had permeabilities $K/H^2 = 0.78 \times 10^{-5}$–$3.7 \times 10^{-5}$, the LP case is in the range of the experimental conditions, while the other cases are more permeable than the experimentally applied media.

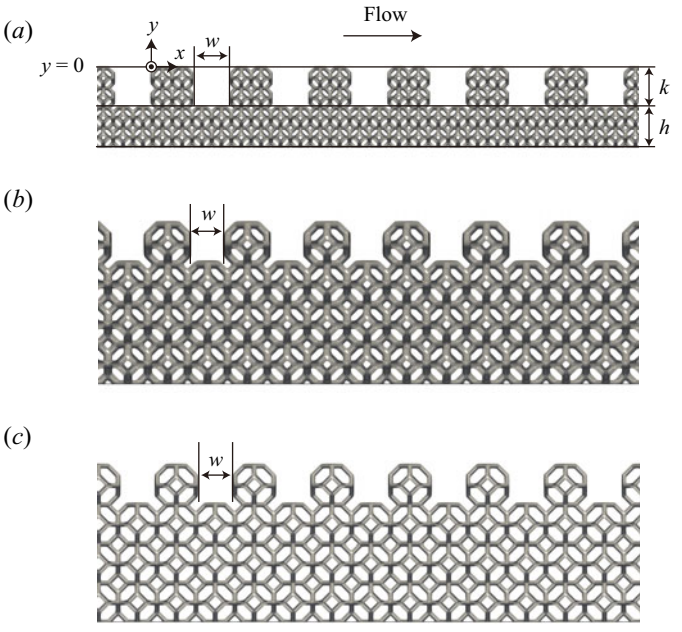

Figure 3. Surface geometries: (*a*) case LP1 with origin of the coordinates, (*b*) case MP1, (*c*) case HP1.

Connecting the Kelvin cells regularly, the rib-roughened porous bed is constructed as shown in figure 3. As for the rib width, although the difference is very slight, the exact rib width is $k + d$, which is slightly larger than the rib height since this study applies Kelvin cells with fully shaped ligaments, while the ligaments of the Kelvin cell shown in figure 1 are cut in half at the surfaces of the unit box. Accordingly, the exact ratios of w/k are not integers, as shown in table 1. The ribs are constructed using one Kelvin cell for the HP and MP cases, while for the LP cases they consist of four cells in the streamwise wall-normal (x–y) sections, as shown in figure 3. Note that because of the open cell structure, the cross-sectional rib shapes may not look square for cases HP1 and MP1. The rib height is hence $k = D$ for both HP and MP cases. Correspondingly, the pore scales of cases HP and MP are the same as the rib height, hence for a designed porosity, they are the maximum pore size, leading to the most permeable structure with the present Kelvin cells for ribbed beds. The porosity is controlled by changing the ligament diameter d in this study. Figure 3(*a*) also shows the origin of the coordinates used in the discussions in this study. As indicated in figure 3, the present porous layer thickness is $h = k$ for case LP, while $h = 3k$ for cases HP and MP. In Appendix B, it is shown that each porous layer thickness hardly affects the turbulence characteristics over the porous bed.

The sizes of the computational box $L_x \times L_y \times L_z$ are listed in table 1. To resolve the porous structures and near-wall turbulence, fine lattice regions with spacings $\Delta^f = \Delta/2$, where Δ is the standard lattice spacing, are applied at the regions below 100 wall units by using the imbalance correction zonal grid refinement method of Kuwata & Suga (2016*a*). Then, for example, the node numbers of the finer and standard lattice regions for case HP are $3299(x) \times 275(y) \times 991(z)$ and $1650(x) \times 295(y) \times 496(z)$, respectively. The corresponding total node numbers are listed in table 1. The lattice resolution for porous media for cases LP, MP and HP is maintained at $d/\Delta^f = 8$, which is confirmed to be fine enough later, in § 3.2. The normalized lattice spacings $(\Delta^f)^+$ are hence always

Case	Re_K	Re_τ	δ_p/k	u_τ^t/U_b	u_*/U_b	u_τ^b/U_b	C_D	κ	d_0^+	h_0^+	k_s^{*+}	δ_r^+
S1	—	224.0	5.03	0.071	0.080	0.084	0.0141	—	—	—	—	—
S9	—	625.5	7.10	0.081	0.157	0.167	0.0556	0.39	83.8	21.6	595	151
LP1	2.2	348.2	5.95	0.076	0.106	0.113	0.0256	0.29	29.4	8.8	100	48
LP9	2.7	487.5	6.61	0.080	0.132	0.141	0.0400	0.24	111.3	46.4	342	158
MP1	5.0	427.2	6.36	0.077	0.121	0.129	0.0331	0.26	57.7	22.4	196	76
MP9	5.2	460.3	6.52	0.078	0.127	0.136	0.0371	0.24	103.5	39.3	302	128
HP1	7.5	471.2	6.58	0.081	0.133	0.142	0.0405	0.23	98.1	45.8	323	119
HP9	7.5	464.8	6.52	0.077	0.126	0.135	0.0362	0.23	123.6	47.7	323	136

Table 2. Calculated flow field parameters. Reynolds numbers are defined as $Re_K = K^{1/2}u_*/\nu$, $Re_\tau = u_*\delta_p/\nu$, where δ_p is the equivalent boundary layer thickness on the porous wall side. The friction velocities u_τ^t, u_* and u_τ^b are defined from the shear stresses at the top wall (τ_t) the rib-top location at $y = 0$ (τ_*) and the rib foot location at $y = -k$ (τ_b), respectively. The parameters κ, d_0, h_0 and k_s^*, are the von Kármán constant, the zero-plane displacement, the roughness scale and the characteristic roughness height, respectively. The nominal roughness sublayer thickness is δ_r. A value normalized by u_* is described as $(\cdot)^+$.

smaller than 2, and owing to the interpolated bounce-back scheme, the averaged distance of the first fluid-phase nodes from the solid parts is approximately less than one wall unit. With this resolution, it is confirmed that the solid ligament boundaries well satisfy no-slip and no-transpiration conditions by the interpolated bounce-back scheme. The present resolution is comparable to those in the previous DNS studies (Chikatamarla *et al.* 2010; Bespalko, Pollard & Uddin 2012; Kuwata & Suga 2016*b*, 2017). Hereafter, $(\cdot)^+$ denotes a normalized value based on the friction velocity u_* at the rib-top location. Pokrajac *et al.* (2006) noted that there had been many discussions to determine the reference friction velocity. There were several candidates, such as the bed shear stress, the total fluid shear stress at the roughness crest, and so on. Note that the total fluid shear stress is the sum of the plane-averaged viscous, Reynolds and dispersion shear stresses. Following Finnigan (2000), Poggi *et al.* (2004), Jarvela (2005), Nakagawa, Tsujimoto & Shimizu (1991), Pokrajac *et al.* (2006), Coceal *et al.* (2007) and Burattini *et al.* (2008), this study defines τ_* as the total fluid shear stress at the roughness crest (rib-top location $y = 0$). The friction velocity u_* ($= \sqrt{\tau_*/\rho}$) listed in table 2 is obtained by the momentum balance, which means that the pressure drop Δp is balanced with the wall-shear stress at the top wall τ_t and the total shear stress τ_* at $y = 0$ as

$$L_x(\tau_t + \tau_*) = (H - k)\,\Delta p. \tag{3.1}$$

The statistical quantities are obtained through at least 33 turnover times after the simulated variables become free from the initial conditions. Although the time step δt is unity in the normalized lattice Boltzmann equation, depending on the present cases it is equivalent to $1.1 \times 10^{-5}H/u_*$–$3.3 \times 10^{-5}H/u_*$ in the physical space. Accordingly, 21 000–48 000 time steps are required for one turnover time.

3.2. *Boundary conditions and validation of computational lattices*

The no-slip flow boundary conditions at the ligament surfaces of the Kelvin cells are imposed by the linear interpolated bounce-back condition (Pan *et al.* 2006) using the level set functions that indicate the distance from solid surfaces. At the upper and very bottom no-slip walls of the channel located at $y = 0.9H$ and $y = -(k + h)$, respectively, the halfway bounce-back condition is applied. The periodic flow conditions are imposed

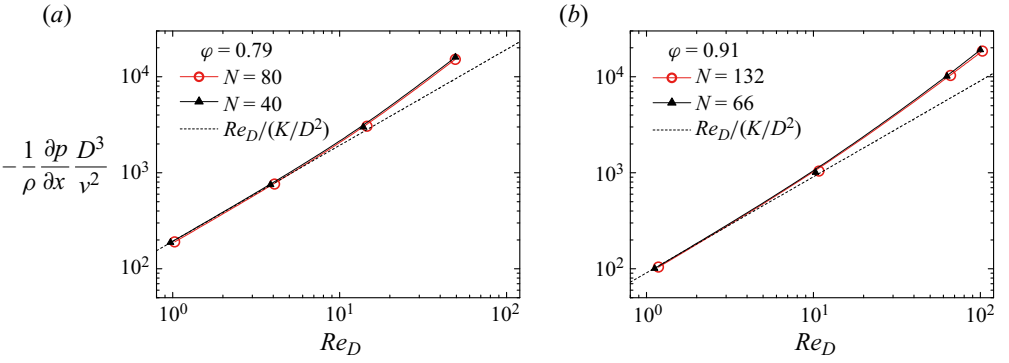

Figure 4. Pressure gradient versus cell Reynolds number, for (*a*) $\varphi = 0.79$, (*b*) $\varphi = 0.91$. The cell Reynolds number is $Re_D = U_D D/\nu$, with the Darcy velocity U_D. The grid resolution N corresponds to the grid number for each direction. The dotted lines correspond to the Darcy law.

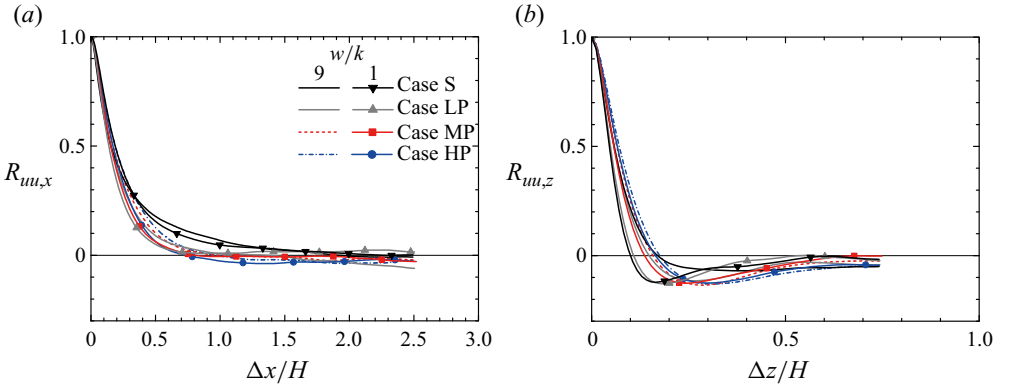

Figure 5. Two-point spatial correlation functions of the streamwise velocity fluctuations at $y = k$: (*a*) streamwise two-point correlations; (*b*) spanwise two-point correlations.

on the streamwise and spanwise directions at the computational box surfaces. A constant streamwise pressure difference is also imposed between the inlet and outlet boundaries.

In the preliminary discussion, we checked the effects of the lattice resolution and the computational box size. Computations using a unit cell with a fixed pressure drop and the periodic velocity boundary condition for each direction are carried out to see the lattice node dependency. Figure 4 compares profiles of the pressure gradient versus the cell Reynolds number depending on the lattice resolution. For each porosity case, the resolution N corresponds to the lattice number dividing each side of the unit cell: $N = D/\Delta$, where Δ is the lattice spacing. Accordingly, $d/\Delta = 8$, 16 lead to $N = 40$, 80 for $\varphi = 0.79$, while they correspond to $N = 66$, 132 for $\varphi = 0.91$. It is seen that the compared profiles almost perfectly collapse onto each other, and this confirms that the lattice resolution of $d/\Delta = 8$ is fine enough for the simulation around the Kelvin cells. From these computations, the permeability K is obtained by the Darcy law that corresponds to the dotted lines in figure 4. Figure 5 compares the profile of R_{uu,x_i} obtained with the computational box applied to each case at the location a little above $y = k$. The definition of the two-point spatial correlation function of the velocity component u is

$$R_{uu,x_i} = \frac{\overline{u'(x_i)\,u'(x_i + \Delta x_i)}}{\overline{u'(x_i)\,u'(x_i)}}, \tag{3.2}$$

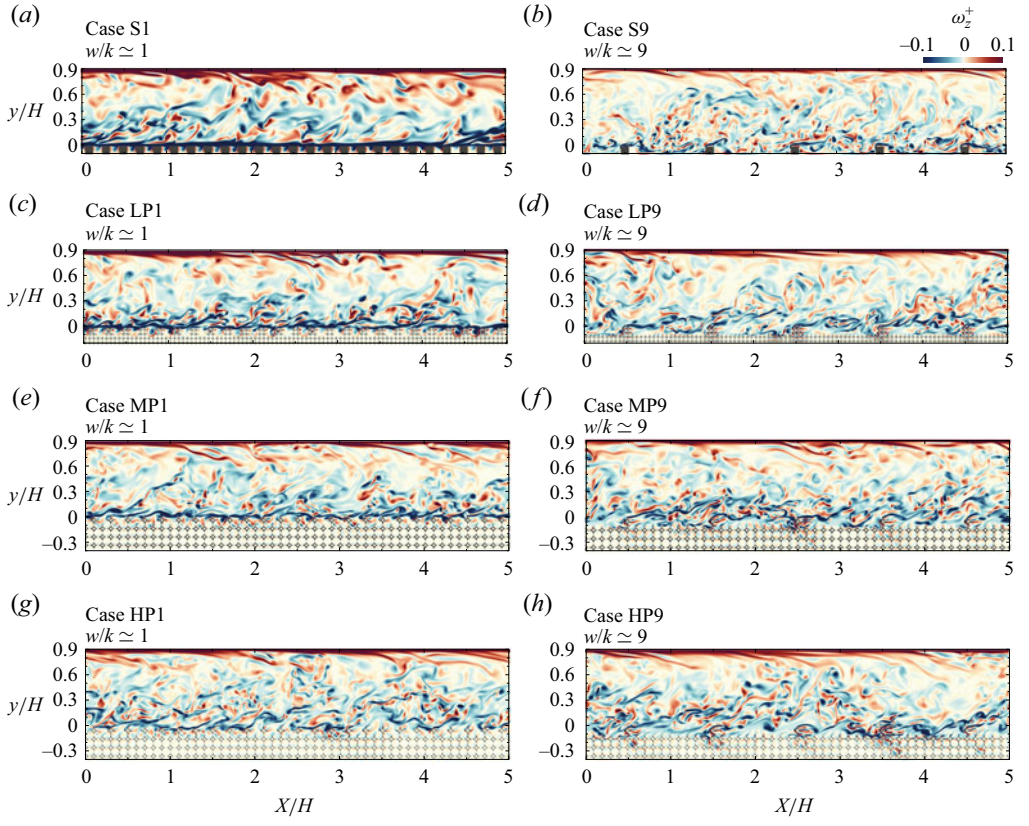

Figure 6. Examples of snapshots for instantaneous vorticity ω_z^+ distributions in streamwise–wall-normal planes. In case HP1, the vorticity distribution near the ribs and core flow region look similar. Although we see smaller pointed vortices near the ribs in case S9, vortices near the ribs look expanded towards the core flow region in cases HP1 and HP9. The origin of the streamwise axis X is set at the inlet of the computational box.

where Δx_i is the distance between the two locations in the x_i-direction. Here, $(x_1, x_2, x_3) = (x, y, z)$. Figure 4($a$) indicates that $R_{uu,x}$ decays monotonically to nearly zero by $\Delta x/H \simeq 2.0$ in each computational box. This suggests that a streamwise box length that is larger than $4.0H$ is satisfactory, and confirms that the length of the present box is reasonable. Since there is no obvious minimum point of each profile, coherent transverse structures are hardly detected. For the spanwise direction, figure 4(b) indicates that $R_{uu,z}$ decays to reasonably small values by $\Delta z/H \simeq 0.7$ in all computational boxes. The spanwise size $1.5H$ of the present standard box is hence confirmed to be reasonable. It is then confirmed that the presently applied lattice resolutions and computational box sizes listed in table 1 are reasonable for the following discussion.

4. Results and discussion

4.1. *General flow patterns*

To obtain general ideas for turbulence structures of the present simulations, figure 6 shows examples of images for the instantaneous spanwise vorticity ω_z^+ distributions. Clearly, the flow image for case S1 at $w/k \simeq 1$ is very different from the other images, and its distribution patterns look quite symmetrical over the rib-top region in the X–y plane.

At $w/k \simeq 1$ as the permeability increases, the concentration of strong vortices near the ribs becomes relaxed, and the vorticity distribution in the near-rib region tends to be similar to that in the core region for case HP1. As for $w/k \simeq 9$, strong smaller vortices near the ribs look expanded towards the core region depending on the increment of the permeability. These observations imply that turbulence levels near the ribs are large and expanded wider towards the channel centre in the permeable cases at both rib spacings.

For the time-mean statistical flow patterns, figure 7 shows the streamlines for each case. The streamlines are presented by plotting contour lines of the stream functions calculated from spanwise-averaged time-mean velocities. Since the purpose of these plots is to show general flow patterns, the lines are drawn with arbitrary spacings. Obviously, the flow patterns in permeable cases change from those of the impermeable cases depending on the permeability. This trend is consistent with that reported by Okazaki *et al.* (2022). At $w/k \simeq 1$, as shown in figures 7(*e*,*g*), there is no obvious mean recirculation behind the ribs in cases MP1 and HP1, while it exists clearly in each cavity between the ribs in case LP1. The permeability Reynolds numbers listed in table 2 are $Re_K = 2.2$, 5.0 and 7.5 for cases LP1, MP1 and HP1, respectively. This implies that the mean recirculation bubbles between the ribs, which seem to be typical d-type recirculation bubbles isolated from outflows like that in case S1 and those in Cui *et al.* (2003) and Leonardi *et al.* (2003, 2004), tend to vanish when Re_K becomes larger. (Note that we do not mention small vortices behind ligaments of the Kelvin cells.)

At $w/k \simeq 9$, in figure 7(*d*) it is observed that the mean recirculation flow submerges into the porous bottom layer at $4 < x/k < 9$ in case LP9. Compared with the flow pattern in the impermeable case shown in figure 7(*b*), the centre position of the recirculation shifts downstream, and the length of the recirculation bubble becomes longer. With the increased permeability the mean recirculation submerges into the porous layer in cases MP9 and HP9, as shown in figures 7(*f*,*h*), and we can observe the downward flow underneath the rib, which then goes upwards in between the ribs due to the recirculation inside the porous layer. These recirculation bubbles are exposed to outflows as in case S9 and those seen in the k-type rough wall flows of Cui *et al.* (2003), Leonardi *et al.* (2003) and Ashrafian *et al.* (2004). The observed trends of the flow patterns over the porous layers shown in figures 7(*d*,*f*,*h*) agree well with the experimentally reported trends by Okazaki *et al.* (2020). The permeability Reynolds numbers listed in table 2 are $Re_K = 2.7$, 5.2 and 7.5 for cases LP9, MP9 and HP9, respectively. Hence the blocking effect by the rib that keeps mean recirculation bubbles over the porous layer becomes weak, and the recirculation bubbles tend to vanish as Re_K increases.

4.2. *Statistical flow characteristics*

First, figure 8 compares the present and experimental data at comparable permeability Reynolds numbers since we consider that Re_K is a measure to characterize the present flow trends as discussed in the later sections. The presented profiles in figures 8(*a*,*c*) are the streamwise–spanwise plane-averaged time-mean streamwise velocities (for simplicity hereafter, mean velocities)

$$\langle U \rangle = \epsilon \langle U \rangle^f = \frac{\epsilon}{S^f} \int_{S^f} \bar{u} \, \mathrm{d}s, \tag{4.1}$$

normalized by the bulk mean velocity U_b, that is,

$$U_b = \frac{1}{H} \int_{-k}^{H-k} \langle U \rangle \, \mathrm{d}y, \tag{4.2}$$

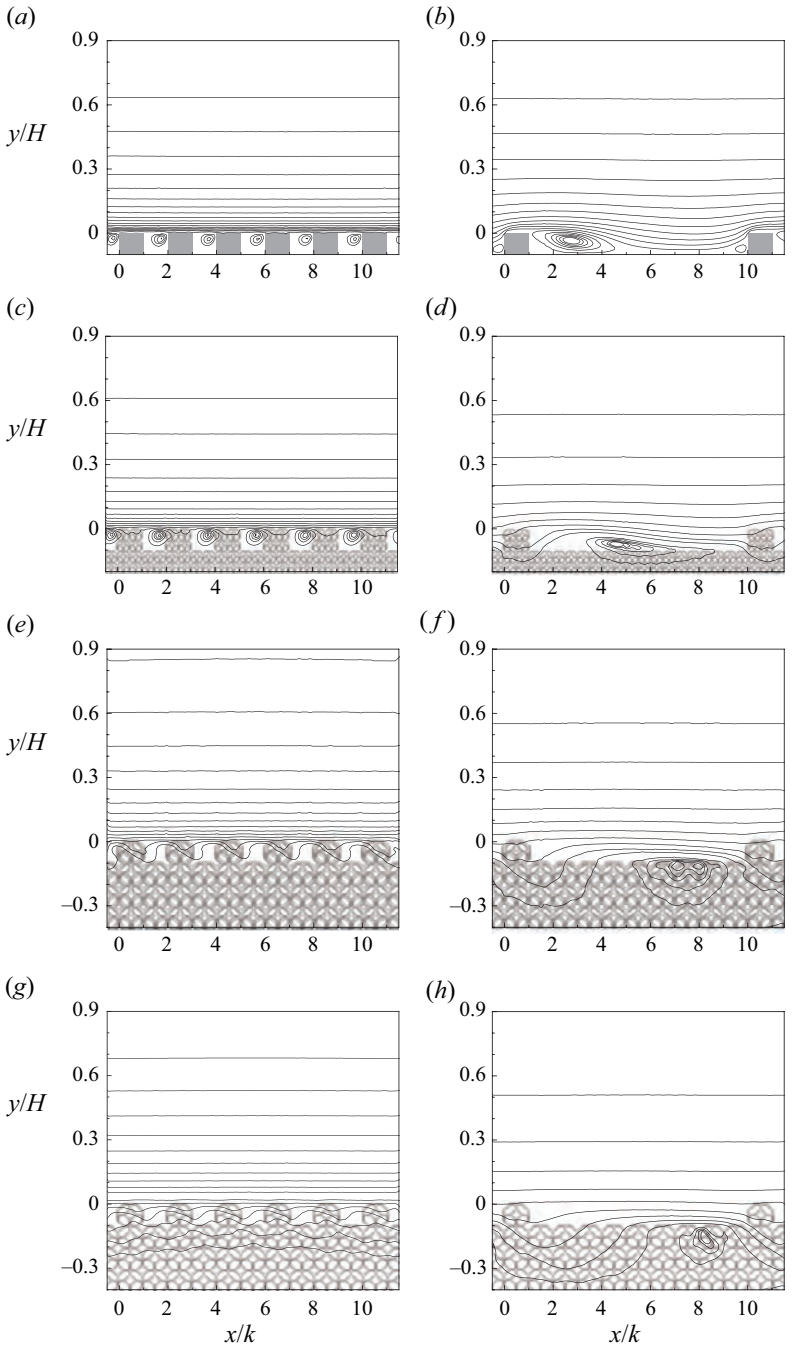

Figure 7. Spanwise averaged time-mean streamlines: (*a*) case S1, (*b*) case S9, (*c*) case LP1, (*d*) case LP9, (*e*) case MP1, (*f*) case MP9, (*g*) case HP1, (*h*) case HP9. The lines are drawn with arbitrary spacings.

where S is an x–z plane area, ϵ is the fluid-phase ratio of the plane area, $\overline{(\cdot)}$ denotes a time-mean variable, and $(\cdot)^f$ denotes a fluid-phase variable. A fluid-phase plane-averaged value of ϕ is denoted as $\langle\phi\rangle^f$, and a superficially plane-averaged value of ϕ is $\langle\phi\rangle$, hereafter. The relation between those variables is $\langle\phi\rangle = \epsilon\langle\phi\rangle^f$. Figures 8(*b*,*d*)

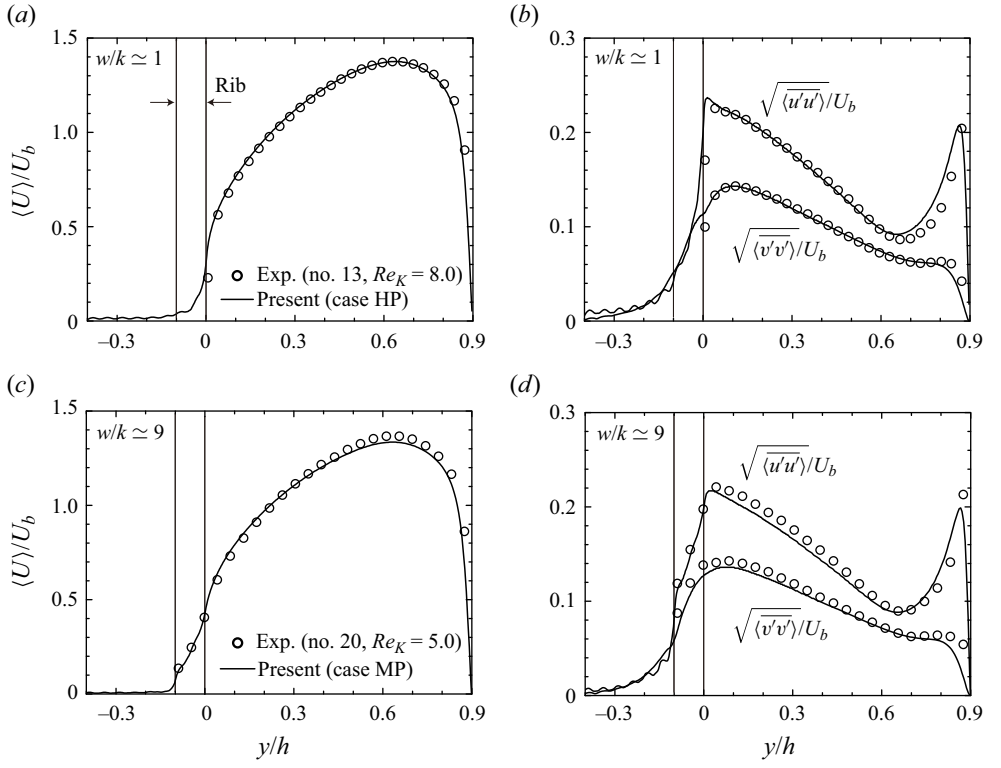

Figure 8. Comparison with the experimental data of mean velocity and r.m.s. velocities: (*a*,*b*) $w/k \simeq 9$ at $Re_K \simeq 5$; (*c*,*d*) $w/k \simeq 1$ at $Re_K \simeq 8$. Experimental data are from Okazaki *et al.* (2022). The experimental porous media nos 13 and 20 were metallic foam media with porosity $\varphi = 0.95$.

indicate the plane-averaged root mean square (r.m.s.) velocities, where $u_i' = u_i - \bar{u}_i$, with $(u_1, u_2, u_3) = (u, v, w)$. Although the compared cases are representative, the shown agreement confirms that the present simulation data are useful to elucidate the turbulent flow physics which governs the rib-roughened porous wall flows studied experimentally by Okazaki *et al.* (2022).

Figure 9 compares the simulated mean velocity profiles. It is seen that the mean velocity increases below the rib-top position ($y < 0$) as the permeability increases for both $w/k \simeq 1$ and 9. Because of this increase of the flow rate at $y < 0$, the velocity profile reduces above the rib-top region while it recovers in the upper half-region. These observed trends are consistent with those shown in the experiments by Okazaki *et al.* (2022). As for the velocity magnitudes at the rib-bottom position $y/H = -0.1$, they are very minor even at $w/k \simeq 9$ in case HP. This contrasts with the existence of substantial slip velocities at flat porous interfaces. Indeed, Suga *et al.* (2010) and Efstathiou & Luhar (2018) reported that at 'flat' porous interfaces, there existed substantial slip velocities that were approximately 30 % of the bulk or free-stream velocity. (Interestingly, the velocity magnitudes at the rib-top position $y = 0$ are, however, close to those slip velocities.) Accordingly, although flow penetration into the porous layer at $y/H < -0.1$ is observed in permeable cases, it looks very small both at $w/k \simeq 1$ and 9. This indicates that although streamlines are drawn inside the porous bed in figure 7, the flow rate there is negligibly small.

The profiles of the plane-averaged Reynolds shear stress (for simplicity, Reynolds shear stress hereafter) and dispersion shear stress are shown in figure 10. Here, the velocity

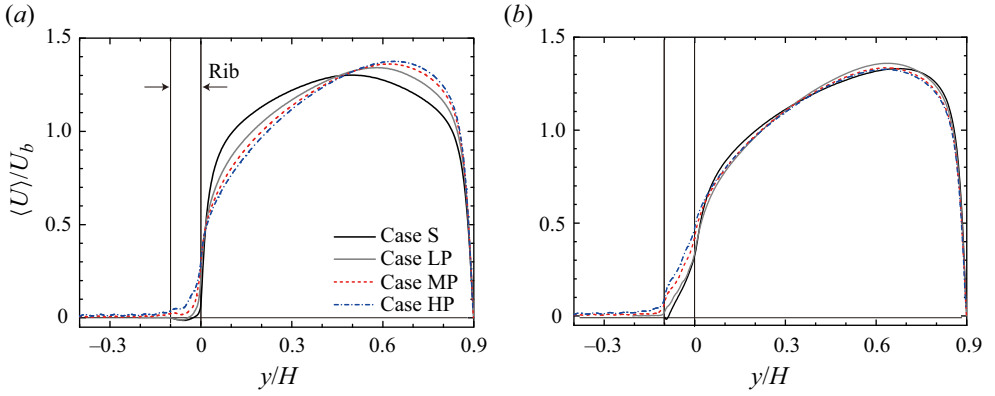

Figure 9. Comparison of plane-averaged time-mean velocities: (*a*) streamwise mean velocities at $w/k \simeq 1$; (*b*) streamwise mean velocities at $w/k \simeq 9$.

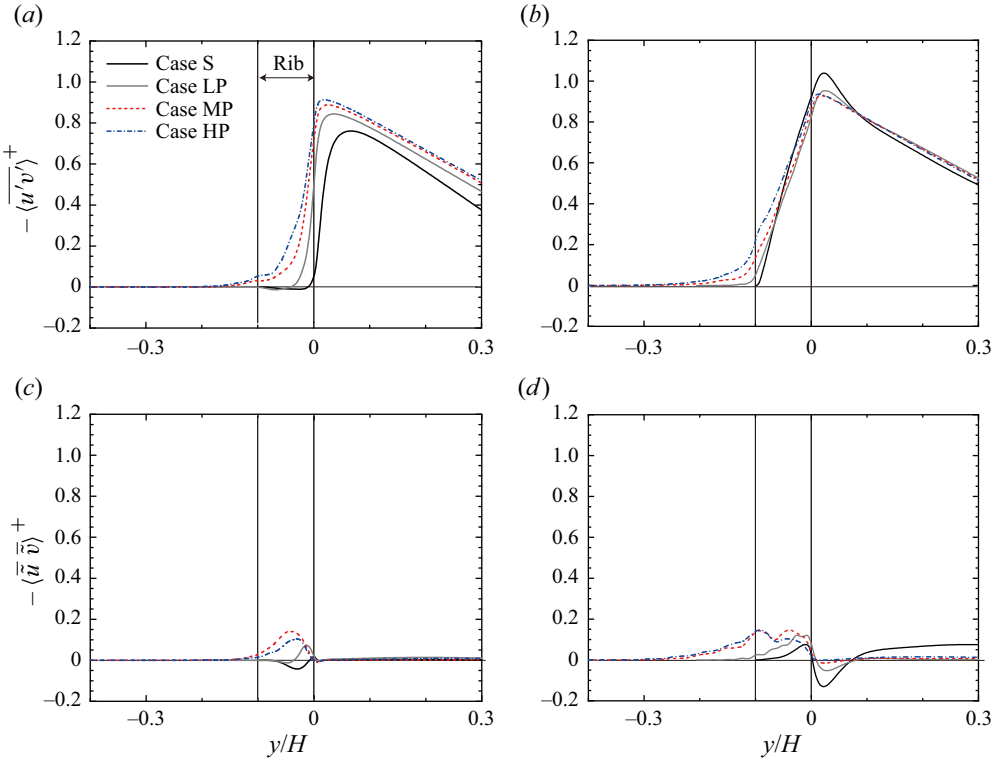

Figure 10. Comparison of plane-averaged Reynolds shear and dispersion shear stresses: (*a*) Reynolds shear stresses at $w/k \simeq 1$; (*b*) Reynolds shear stresses at $w/k \simeq 9$; (*c*) dispersion stresses at $w/k \simeq 1$; (*d*) dispersion stresses at $w/k \simeq 9$.

dispersion is $\tilde{\bar{u}}_i = \bar{u}_i - \langle \bar{u}_i \rangle^f$, and the dispersion stress is defined as

$$\langle \tilde{\bar{u}}_i \tilde{\bar{u}}_j \rangle = \frac{\epsilon}{S^f} \int_{S^f} \left(\bar{u}_i - \langle \bar{u}_i \rangle^f \right) \left(\bar{u}_j - \langle \bar{u}_j \rangle^f \right) \mathrm{d}s. \tag{4.3}$$

At $w/k \simeq 1$, as the permeability increases, the Reynolds shear stress around the rib increases monotonically as shown in figure 10(a). This implies that turbulence is enhanced as the permeability increases. For $w/k \simeq 9$, shown in figure 10(b), such a trend is seen only in the region near the rib-bottom. At the rib-top position, the Reynolds shear stress of case S9 is predominant over the other cases, while the profiles of the permeable cases look almost collapsed to a single profile. This suggests that the turbulence level over the rib at $w/k \simeq 9$ is rather insensitive to the present permeable cases once normalized by the friction velocity. Moreover, the levels of cases HP1 and HP9 over the ribs become almost the same, and this suggests that the rib spacing becomes ineffective to affect turbulence over the ribs at a higher permeability case. As indicated in figure 9(a), in case S1, the magnitude of $\langle U\rangle/U_b$ between the ribs is close to zero, though there are locally negative velocities due to the recirculation bubbles as seen in figure 7(a). Correspondingly, $-\langle\tilde{\tilde{u}}\tilde{\tilde{v}}\rangle^+$ shows a negative profile below the rib-top. As the permeability increases, however, such negative local velocities tend to disappear. Similar things take place just over the ribs in case S9. Accordingly, as the permeability increases, the dispersion shear stress changes its sign near the rib, as seen in figures 10(c,d). The penetration of the shear stress is observed until $y/H \simeq -0.3$ in case HP9, unlike in the mean velocity profile. As for the dispersion stress, although its maximum magnitude is 10–20 % of that of the Reynolds shear stress, its levels inside the porous layer at $y/H < -0.1$ become comparable or even larger than those of the Reynolds shear stress for permeable cases MP9 and HP9, as seen in figure 10(d). These trends suggest that surface mass transfer at $y/H < -0.1$ by turbulence and dispersion clearly increases as the increase of the permeability at $w/k \simeq 9$.

Figures 11 and 12 indicate the simulated r.m.s. velocities and r.m.s. dispersion velocities, respectively. At $w/k \simeq 1$, the trends of the r.m.s. streamwise velocities over the rib-top position shown in figure 11(a) look different from those in the Reynolds shear stress profiles, while the other components shown in figures 11(c,e) behave similarly to the Reynolds shear stress. The streamwise component of case S1 is larger than in the other cases just above the rib, while the wall-normal and spanwise components of case S1 are smaller than in the other cases. This means that turbulence anisotropy there in case S1 is higher than that in the other cases. Turbulence anisotropy over the rib hence reduces clearly in permeable cases since the permeability weakens turbulence anisotropy near the porous interface (Breugem *et al.* 2006; Suga *et al.* 2010). At $w/k \simeq 9$, although there are slight discrepancies between the cases, the general trends of the cases look similar to one another. These trends over the rib are also observed in Okazaki *et al.* (2020). The penetration depths of permeable cases are similar to each other for $w/k \simeq 1$ and 9 unlike in the Reynolds shear stress profiles, and the permeability enhances the r.m.s. velocities inside the porous layer at $y/H < -0.1$. This implies that inside the porous layer, the wall-normal fluctuating energy induced by the vertical pressure fluctuation is redistributed to the other components. The r.m.s. dispersion velocities inside the porous layer at $y/H < -0.1$ shown in figure 12 at $w/k \simeq 9$ are clearly larger than those at $w/k \simeq 1$, unlike the r.m.s. velocities. This trend corresponds to the mean streamlines presented in figure 7. Particularly at $w/k \simeq 9$, since the mean recirculating flow with certain magnitudes of local velocities exists inside the porous layer, the r.m.s. dispersion velocities exist. While the magnitudes of the r.m.s. dispersion velocities inside the porous layer at $w/k \simeq 9$ tend to be large in the larger permeable cases, those in cases MP9 and HP9 look similar to each other. Such a trend is also seen in the dispersion stress shown in figure 10(d). (Although there seem to be several reasons why this happens, such as the porosity and thickness of the porous layer, we do not discuss this issue further since our main focus is on the flow physics over porous

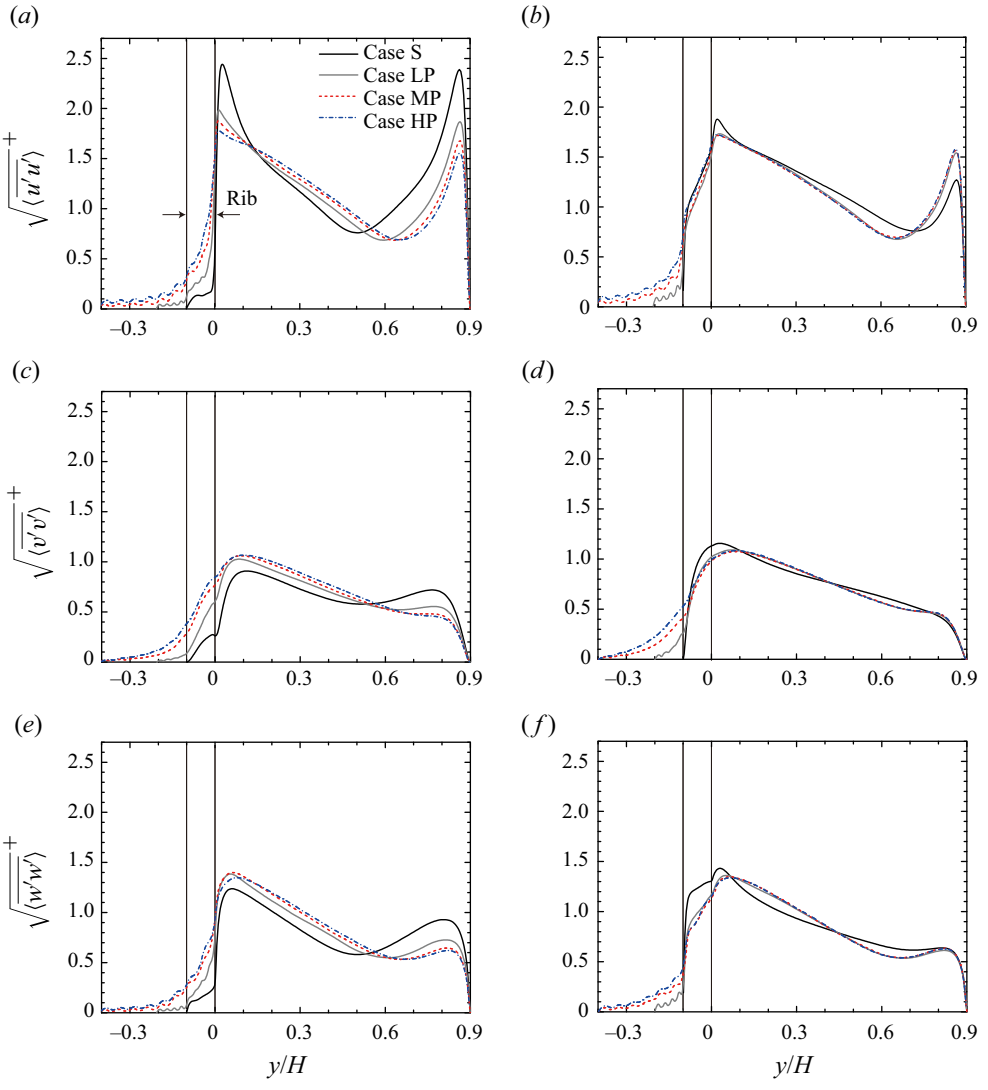

Figure 11. Comparison of plane-averaged r.m.s. velocities: (*a*) streamwise r.m.s. velocities at $w/k \simeq 1$; (*b*) streamwise r.m.s. velocities at $w/k \simeq 9$; (*c*) wall-normal r.m.s. velocities at $w/k \simeq 1$; (*d*) wall-normal r.m.s. velocities at $w/k \simeq 9$; (*e*) spanwise r.m.s. velocities at $w/k \simeq 1$; (*f*) spanwise r.m.s. velocities at $w/k \simeq 9$.

rib roughness. Note that as confirmed in Appendix B, the presently applied porous layer thicknesses are enough to discuss turbulence over porous rib roughness keeping it free from the effects of the very bottom wall.) The trends observed above suggest that mass flux across the porous surface towards the inside region would be significantly larger at $w/k \simeq 9$ than at $w/k \simeq 1$, owing to the dispersion rather than turbulence.

4.3. *Drag characteristics*

Corresponding to the trend of turbulence quantities observed in figures 10 and 11, the drag shows characteristic behaviours as seen in figure 13(*a*) that compares the data with the experiments of Okazaki *et al.* (2022). The rib-bottom drag coefficient C_D corresponds to

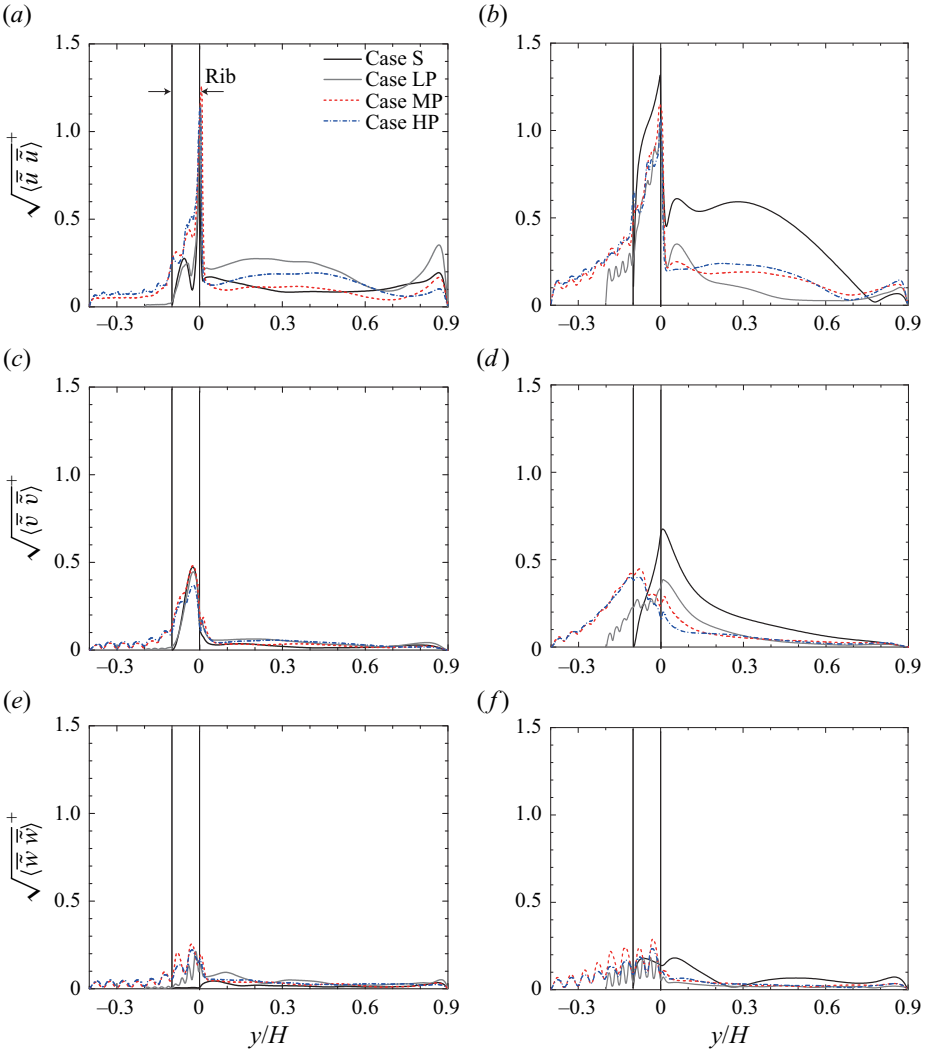

Figure 12. Comparison of r.m.s. dispersion velocities: (*a*) streamwise components at $w/k \simeq 1$; (*b*) streamwise components at $w/k \simeq 9$; (*c*) wall-normal components at $w/k \simeq 1$; (*d*) wall-normal components at $w/k \simeq 9$; (*e*) spanwise components at $w/k \simeq 1$; (*f*) spanwise components at $w/k \simeq 9$.

the sum of the frictional and pressure drag coefficients described by Leonardi *et al.* (2003), who simulated solid impermeable cases, and their data are also included in figure 13(*a*). In the present study, the definition is $C_D = 2\tau_b/(\rho U_b^2)$, where the drag over the rib-bottom τ_b is calculated by

$$\tau_b = \left(H - \int_{-k}^{0} (1-\epsilon)\,\mathrm{d}y \right) \frac{\Delta p}{L_x} - \tau_t, \tag{4.4}$$

since the joint integration of τ_b and the wall shear stress on the top smooth wall τ_t balances with the integration of the pressure drop over the rib-bottom. The area over which the pressure drop is integrated is proportional to H minus the streamwise–spanwise plane-averaged solid-phase part of the rib height: $\int_{-k}^{0}(1-\epsilon)\,\mathrm{d}y$. Hence C_D here does not

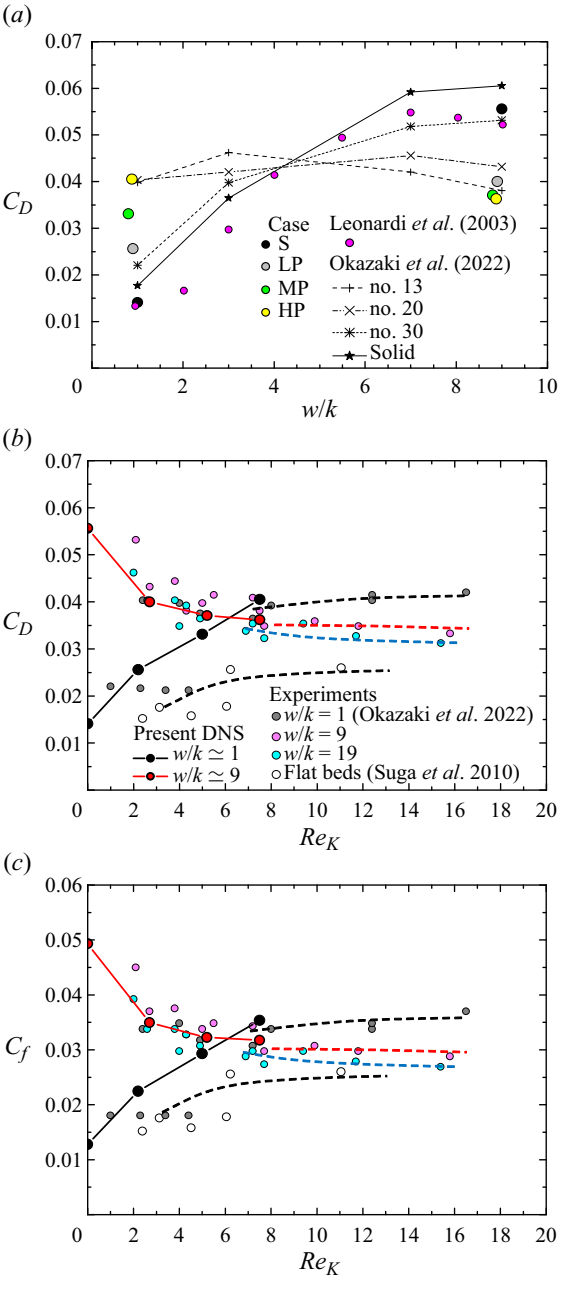

Figure 13. Comparison of the rib-bottom drag coefficients. (*a*) Plots of C_D against the variation of w/k; experimental results are at $Re_b \simeq 5000$ from Okazaki *et al.* (2022). The permeabilities of nos 13, 20 and 30 metallic foam media are $K/k^2 = 3.67 \times 10^{-3}$, $K/k^2 = 1.44 \times 10^{-3}$ and $K/k^2 = 7.78 \times 10^{-4}$, respectively, while their porosity is $\varphi = 0.95$. The DNS data of the impermeable case by Leonardi *et al.* (2003) are at $Re_b \simeq 7000$. (*b*) Plots of C_D against the variation of Re_K; skin friction coefficient C_f at the porous surface is used for the flat bed cases. Each broken curve is an approximate curve for each rib spacing. (*c*) Plots of C_f against the variation of Re_K; here, C_f is defined as $C_f = 2\tau_*/(\rho U_b^2)$.

include the drag by the porous bottom layer below the rib-bottom, but it includes the pressure and frictional drag through the ribs. It is seen that C_D values of the impermeable cases are in close agreement at $w/k \simeq 1$ and 9, while some Reynolds number effects may exist at $w/k \simeq 9$. In both the present and experimental studies, as the permeability (and thus Re_K) increases, C_D increases at $w/k \simeq 1$, although the reverse trend is seen at $w/k \simeq 9$, while the differences are small between the present permeable cases. These observed trends correspond qualitatively to the changes of the permeability Reynolds number. In figure 13(*b*), however, we understand that the correlation between C_D and Re_K is not general when experimental data are cross-plotted. Note that the experimental values shown in figures 13(*b*,*c*) are somewhat dispersed, particularly at the low Re_K region. As reported in the experiments for flat porous beds by Suga *et al.* (2010) and Suga, Mori & Kaneda (2011), the slippage velocity at the porous interface and the near-wall characteristics of permeable wall turbulence change drastically in the low Re_K region, particularly below $Re_K \simeq 3$. Because of this, the data of Suga *et al.* (2010) were scattered, though the general trend looked obvious. Accordingly, the measured values of Okazaki *et al.* (2022) look dispersed in the low Re_K region. Such a trend looks somehow exaggerated at $w/k = 1$. As Re_K becomes large, there exist asymptotic limiting values of C_D that are independent of Re_K but dependent on the rib spacing. To exclude explicit effects of the pressure drag from the discussion, in figure 13(*c*) we plot the distributions of C_f, which is presently defined as $C_f = 2\tau_*/(\rho U_b^2)$. Since the general trends shown in figure 13(*c*) are the same as those shown in figure 13(*b*), it is clear that the effects of rib spacing affect the flows over the ribs dynamically. To understand further how the rib-bottom drag is characterized from a phenomenological viewpoint, C_D is next decomposed as in Fukagata, Iwamoto & Kasagi (2002).

The x–z plane-averaged time-mean momentum equation for the present flows may be written as

$$0 = -\frac{\epsilon}{\rho}\frac{\partial \langle \bar{p} \rangle^f}{\partial x} + \frac{\partial}{\partial y}\left(\nu \frac{\epsilon \langle \bar{u} \rangle^f}{\partial y}\right) - \bar{f}_1 - \frac{\partial}{\partial y}(R_{12} + T_{12}), \tag{4.5}$$

where $\bar{f}_1$, R_{12} and T_{12} are the drag force, Reynolds stress and dispersion stress terms, respectively. By integrating (4.5) three times, with the equivalent boundary layer thickness $\delta_p = \tau_*(H-k)/(\tau_* + \tau_t)$, the rib-bottom drag coefficient may be decomposed as

$$C_D = \underbrace{\frac{\Psi}{Re_b}}_{\text{laminar}} \underbrace{- \frac{\Psi}{2U_b^2 H^2}\int_{-k}^{0} (y+k)(y+k-2H)\bar{f}_1 \,\mathrm{d}y}_{\text{rib drag}}$$
$$\underbrace{- \frac{\Psi}{U_b^2 H^2}\int_{-k}^{H-k} (H-k-y) R_{12} \,\mathrm{d}y}_{\text{turbulence}} \underbrace{- \frac{\Psi}{U_b^2 H^2}\int_{-k}^{H-k} (H-k-y) T_{12} \,\mathrm{d}y}_{\text{dispersion}}, \tag{4.6}$$

where Ψ is calculated as

$$\Psi = \left\{ \frac{1}{4} - \frac{\int_{-k}^{0} (H-k-y)^2 \epsilon \,\mathrm{d}y + (H-k)^3/3}{4H^2\left(\int_{-k}^{0} \epsilon \,\mathrm{d}y + \delta_p\right)} \right\}^{-1}, \tag{4.7}$$

since $\epsilon = 1$ at $y > 0$. The derivation process of (4.6) and (4.7) is detailed in Appendix C. Figure 14 shows the breakdown chart of the rib-bottom drag coefficient. At both $w/k \simeq 1$

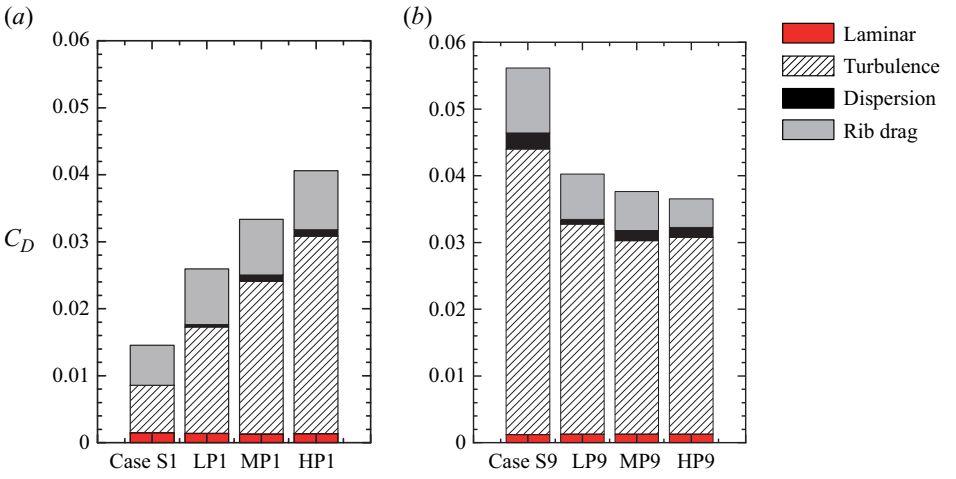

Figure 14. Breakdown of the rib-bottom drag coefficient. (*a*) Factors for $w/k \simeq 1$: S1 (laminar 1.49×10^{-3}, turbulence 7.03×10^{-3}, dispersion -3.90×10^{-5}, rib drag 5.98×10^{-3}); LP1 (laminar 1.37×10^{-3}, turbulence 1.59×10^{-2}, dispersion 3.54×10^{-4}, rib drag 8.31×10^{-3}); MP1 (laminar 1.29×10^{-3}, turbulence 2.28×10^{-2}, dispersion 9.35×10^{-4}, rib drag 8.31×10^{-3}); HP1 (laminar 1.33×10^{-3}, turbulence 2.95×10^{-2}, dispersion 9.67×10^{-4}, rib drag 8.80×10^{-3}). (*b*) Factors for $w/k \simeq 9$: S9 (laminar 1.20×10^{-3}, turbulence 4.28×10^{-2}, dispersion 2.42×10^{-3}, rib drag 9.71×10^{-3}); LP9 (laminar 1.28×10^{-3}, turbulence 3.16×10^{-2}, dispersion 1.13×10^{-3}, rib drag 6.70×10^{-3}); MP9 (laminar 1.28×10^{-3}, turbulence 2.90×10^{-2}, dispersion 1.51×10^{-3}, rib drag 5.85×10^{-3}); HP9 (laminar 1.27×10^{-3}, turbulence 2.95×10^{-2}, dispersion 1.47×10^{-3}, rib drag 4.28×10^{-3}).

and 9, the laminar part, which is Ψ/Re_b in (4.6), does not change visibly in the simulated cases since Ψ does not change very much. Indeed, $\Psi = 6.9$–7.4 in the range $\delta_p/H = 0.4$–0.7. The other parts, however, change depending on the permeability and the rib spacing. At $w/k \simeq 1$, the increment of the turbulence part looks sensitive to the increase of the permeability, while the rib-drag part does not look so sensitive. Indeed, although the rib-drag part is slightly larger in the permeable cases, its behaviour is not monotonic. The pressure drag and the skin friction inside the ribs, which compose the rib drag, change depending on the permeability. The former decreases owing to the permeability, while the latter increases as the flow rate through the ribs, as implied in figure 7. The dispersion part is not significant owing to the dispersion shear stress, which is not significant compared with the Reynolds shear stress, as shown in figure 10. Accordingly, the main factor of the increase of C_D at $w/k \simeq 1$ depending on the permeability is the turbulence part.

At $w/k \simeq 9$, the rib-drag part clearly decreases depending on the permeability. This suggests that the decrease of the pressure drag depending on the permeability is more significant than the increase of the skin friction. The dispersion part becomes larger than that at $w/k \simeq 1$, while its behaviour does not seem to relate to the permeability. As at $w/k \simeq 1$, the turbulence part is most dominant and determines the general trend of C_D. Interestingly, the magnitudes of the turbulence parts in cases HP1, LP9, MP9 and HP9 are at the same level. This implies that the turbulence structure may be similar in those cases. Note that the experiments by Suga *et al.* (2010) for the ribless flat cases, in which the rib-drag and dispersion parts do not appear, reported much less surface friction, as shown in figure 13(*b*). This suggests that when we gradually increase the rib spacing to $w/k \to \infty$, the magnitudes of the turbulence part and rib-bottom drag decrease gradually towards certain levels depending on Re_K.

To understand the mutual dependency between the breakdown factors shown in figure 14, we consider the budget equations of the dispersion and Reynolds stresses appearing in (4.5). Following Kuwata & Suga (2013, 2015) and Kuwata, Suga & Sakurai (2014), by the double (time and plane) averaging theory (Whitaker 1996), the budget equations of the dispersion and Reynolds stresses are derived as below. For $\left\langle \bar{\tilde{u}}_i \bar{\tilde{u}}_j \right\rangle^f$, which corresponds to T_{ij}/ϵ,

$$
\begin{aligned}
0 = {} & \underbrace{\frac{\partial}{\partial x_k}\left(\nu \frac{\partial \left\langle \bar{\tilde{u}}_i \bar{\tilde{u}}_j \right\rangle^f}{\partial x_k} \right)}_{\text{viscous diffusion}} - \underbrace{2\nu \left\langle \frac{\partial \bar{\tilde{u}}_i}{\partial x_k} \frac{\partial \bar{\tilde{u}}_j}{\partial x_k} \right\rangle^f}_{\text{viscous dissipation: } \mathcal{E}_{ij}} \underbrace{+ \bar{f}_i \left\langle \bar{u}_j \right\rangle^f + \bar{f}_j \left\langle \bar{u}_i \right\rangle^f}_{\text{drag force: } \mathcal{F}_{ij}} \\
& \underbrace{- \frac{\partial}{\partial x_k}\left(\left\langle \bar{\tilde{u}}_j \overline{\left\langle u_k' \right\rangle^f \tilde{u}_j'} \right\rangle^f + \left\langle \bar{\tilde{u}}_i \overline{\left\langle u_k' \right\rangle^f \tilde{u}_i'} \right\rangle^f + \left\langle \bar{\tilde{u}}_j \overline{\tilde{u}_k' \tilde{u}_i'} \right\rangle^f + \left\langle \bar{\tilde{u}}_i \overline{\tilde{u}_k' \tilde{u}_j'} \right\rangle^f \right)}_{\text{turbulent diffusion}} \\
& \underbrace{- \frac{\partial}{\partial x_k}\left(\left\langle \bar{\tilde{u}}_i \bar{\tilde{u}}_j \bar{\tilde{u}}_k \right\rangle^f \right)}_{\text{dispersive diffusion}} \underbrace{- \frac{1}{\rho}\left(\frac{\partial \left\langle \bar{\tilde{u}}_i \bar{\tilde{p}} \right\rangle^f}{\partial x_j} + \frac{\partial \left\langle \bar{\tilde{u}}_j \bar{\tilde{p}} \right\rangle^f}{\partial x_i} \right) + \left\langle \frac{\bar{\tilde{p}}}{\rho}\left(\frac{\partial \bar{\tilde{u}}_i}{\partial x_j} + \frac{\partial \bar{\tilde{u}}_j}{\partial x_i} \right) \right\rangle^f}_{\text{pressure correlation: } \Pi_{ij}^d} \\
& \underbrace{- \left\langle \bar{\tilde{u}}_i \bar{\tilde{u}}_k \right\rangle^f \frac{\partial \left\langle \bar{u}_j \right\rangle^f}{\partial x_k} - \left\langle \bar{\tilde{u}}_j \bar{\tilde{u}}_k \right\rangle^f \frac{\partial \left\langle \bar{u}_i \right\rangle^f}{\partial x_k}}_{\text{mean shear production: } \mathcal{P}_{ij}} \underbrace{- \overline{\left\langle \bar{\tilde{u}}_i \tilde{u}_k' \right\rangle^f \frac{\partial \left\langle u_j' \right\rangle^f}{\partial x_k}} - \overline{\left\langle \bar{\tilde{u}}_j \tilde{u}_k' \right\rangle^f \frac{\partial \left\langle u_i' \right\rangle^f}{\partial x_k}}}_{\text{turbulent shear production: } \mathcal{P}_{ij}^t} \\
& \underbrace{+ \left\langle \left(\overline{\tilde{u}_i' \tilde{u}_k'} + \overline{\tilde{u}_i' \left\langle u_k' \right\rangle^f} \right) \frac{\partial \bar{\tilde{u}}_j}{\partial x_k} \right\rangle^f + \left\langle \left(\overline{\tilde{u}_j' \tilde{u}_k'} + \overline{\tilde{u}_j' \left\langle u_k' \right\rangle^f} \right) \frac{\partial \bar{\tilde{u}}_i}{\partial x_k} \right\rangle^f}_{\text{counterpart of } P_{ij}^d \text{ in Reynolds stress}}, \qquad (4.8)
\end{aligned}
$$

while for $\langle \overline{u_i' u_j'} \rangle^f$, which corresponds to R_{ij}/ϵ,

$$
\begin{aligned}
0 = {} & \underbrace{\frac{\partial}{\partial x_k}\left(\nu \frac{\partial \langle \overline{u_i' u_j'} \rangle^f}{\partial x_k} \right)}_{\text{viscous diffusion}} \underbrace{- 2\nu \left(\overline{\frac{\partial \left\langle u_i' \right\rangle^f}{\partial x_k} \frac{\partial \left\langle u_j' \right\rangle^f}{\partial x_k}} + \overline{\left\langle \frac{\partial \tilde{u}_i'}{\partial x_k} \frac{\partial \tilde{u}_j'}{\partial x_k} \right\rangle^f} \right)}_{\text{viscous dissipation: } \varepsilon_{ij}} \\
& \underbrace{- \frac{\partial}{\partial x_k}\left(\overline{\left\langle u_i' \right\rangle^f \left\langle u_j' \right\rangle^f \left\langle u_k' \right\rangle^f} + \overline{\left\langle \tilde{u}_i' \tilde{u}_j' \tilde{u}_k' \right\rangle^f} \right)}_{\text{turbulent diffusion}}
\end{aligned}
$$

$$
\underbrace{-\frac{\partial}{\partial x_k}\left(\overline{\langle u_i'\rangle^f\left\langle\tilde{u}_j'\tilde{u}_k'\right\rangle^f}+\overline{\left\langle u_j'\right\rangle^f\langle\tilde{u}_i'\tilde{u}_k'\rangle^f}+\overline{\langle u_i'\rangle^f\left\langle\tilde{u}_j'\tilde{\bar{u}}_k\right\rangle^f}+\overline{\left\langle u_j'\right\rangle^f\left\langle\tilde{u}_i'\tilde{\bar{u}}_k\right\rangle^f}\right.}_{\text{dispersive diffusion}}
$$

$$
\underbrace{\left.+\overline{\langle u_i'\rangle^f\left\langle\tilde{\bar{u}}_j\tilde{u}_k'\right\rangle^f}+\overline{\left\langle u_j'\right\rangle^f\left\langle\tilde{\bar{u}}_i\tilde{u}_k'\right\rangle^f}+\overline{\langle u_k'\rangle^f\left\langle\tilde{u}_i'\tilde{u}_j'\right\rangle^f}+\overline{\left\langle\tilde{\bar{u}}_k\tilde{u}_i'\tilde{u}_j'\right\rangle^f}\right)}_{\text{dispersive diffusion}}
$$

$$
\underbrace{-\frac{1}{\rho}\left(\overline{\left\langle u_j'\right\rangle^f\frac{\partial\langle p'\rangle^f}{\partial x_i}}+\overline{\langle u_i'\rangle^f\frac{\partial\langle p'\rangle^f}{\partial x_j}}+\overline{\left\langle\tilde{u}_i'\frac{\partial\tilde{p}'}{\partial x_j}\right\rangle^f}+\overline{\left\langle\tilde{u}_j'\frac{\partial\tilde{p}'}{\partial x_i}\right\rangle^f}\right)}_{\text{pressure correlation: }\Pi_{ij}}
$$

$$
\underbrace{-\overline{\langle u_i'u_k'\rangle}^f\frac{\partial\langle\bar{u}_j\rangle^f}{\partial x_k}-\overline{\langle u_j'u_k'\rangle}^f\frac{\partial\langle\bar{u}_i\rangle^f}{\partial x_k}}_{\text{mean shear production: }P_{ij}}\underbrace{+\overline{\left\langle\tilde{u}_k'\tilde{\bar{u}}_i\right\rangle^f\frac{\partial\left\langle u_j'\right\rangle^f}{\partial x_k}}+\overline{\left\langle\tilde{u}_k'\tilde{\bar{u}}_j\right\rangle^f\frac{\partial\langle u_i'\rangle^f}{\partial x_k}}}_{\text{counterpart of }\mathcal{P}_{ij}^t\text{ in dispersion stress}}
$$

$$
\underbrace{-\left\langle\left(\overline{\tilde{u}_i'\tilde{u}_k'}+\overline{\tilde{u}_i'\langle u_k'\rangle^f}\right)\frac{\partial\tilde{\bar{u}}_j}{\partial x_k}\right\rangle^f-\left\langle\left(\overline{\tilde{u}_j'\tilde{u}_k'}+\overline{\tilde{u}_j'\langle u_k'\rangle^f}\right)\frac{\partial\tilde{\bar{u}}_i}{\partial x_k}\right\rangle^f}_{\text{dispersive shear production: }P_{ij}^d}. \tag{4.9}
$$

When the mean shear $\partial\langle\bar{u}_1\rangle/\partial x_2$ exists, from the budget ((4.8) and (4.9)), the mutual energy transfer cycle between the mean flow, dispersion and turbulence fields may be illustrated as in figure 15. Since only the momentum and dispersion stress equations ((4.5) and (4.8)) include the drag force terms, $\mathcal{F}_{11}=2\bar{f}_1\langle\bar{u}\rangle^f$ in the budget equation of T_{11} solely feeds direct effects of the drag force to the dispersion field, while the turbulence field does not receive any direct contribution from the drag force. Since the enhanced energy of T_{11} is redistributed to the other components by the pressure correlation, the energy gained by $\mathcal{F}_{11}$ is redistributed to T_{22} through Π_{22}^d. Then by $\mathcal{P}_{12}$ with the mean shear, T_{12} is enhanced. The enhanced T_{12} increases T_{11} by $\mathcal{P}_{11}$, and so on. By the dispersive shear production P_{ij}^d (called 'wake production' in canopy flows; Finnigan 2000), the dispersion field feeds energy to the turbulence field, while some energy back-scatter from the turbulence field by $\mathcal{P}_{ij}^t$ exists. The diffusion terms spatially diffuse each stress, and $\mathcal{E}_{ij}$ dissipates some of the kinetic energy. Accordingly, since the drag force has direct relations to the projection area of the roughness elements, the roughness effects on turbulence come through the mean shear and the energy transfer from the dispersion field by P_{ij}^d. As for the mutual energy transfer cycle in the turbulence field, it is achieved by the same manner as in the dispersion field.

In case S1, since figure 9(*a*) implies that the velocity gradient in the rib region $-0.1<y/H<0$ is rather small, the drag force contribution through the mean velocity seems small. Indeed, the corresponding magnitude of the Reynolds shear stress in $-0.1<y/H<0$ is very small, as shown in figure 10(*a*). Moreover in figure 14, the (integrated) dispersion part in case S1 is invisibly small. Note that since the dispersion in the region over the rib-top reflects the skewed streamlines caused by the rib roughness as seen in figure 7, the integrated dispersion includes rib effects not only in the rib region but also in the region above the ribs. This suggests that the rib-roughness effects are merely transferred to the

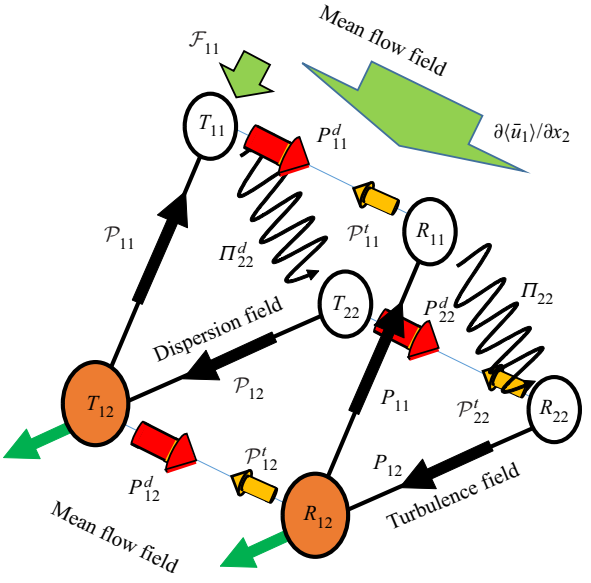

Figure 15. Conceptual illustration of energy flows between mean flow, dispersion and turbulence fields under mean shear. The mean flow field feeds the mean shear $\partial\langle\bar{u}_1\rangle/\partial x_2$ to the dispersion and turbulence fields. The drag force effect is given only to T_{11} through $\mathcal{F}_{11}$. The dispersion and turbulence fields exchange their energy by P^d_{ij} and $\mathcal{P}^t_{ij}$. The dispersion and Reynolds shear stresses (T_{12}, R_{12}) feed back to the mean flow field through the momentum equation. The mean shear production terms ($\mathcal{P}_{ij}$, P_{ij}) are the main sources of the stresses, while the wall-normal components T_{22} and R_{22} do not have the mean shear production. The pressure correlation terms (Π^d_{ij}, Π_{ij}) redistribute energy to the other components (T_{33} and R_{33} are not shown). Although they are not illustrated, the dissipation and diffusion processes exist.

turbulence part of case S1, while the rib-bottom drag includes roughness effects by the rib-drag part, which is not so small. The above consideration is consistent with the fact that turbulence at $w/k = 1$ in the solid case is not characterized by the roughness scale and categorized in the d-type roughness. In the other cases, however, as seen in figures 9 and 14, the mean shear and the dispersion part have certain levels, while they seem quite small in case LP1. Accordingly, the turbulence parts in the permeable cases should have certain effects of roughness scales via the mean shear and dispersion fields. (See figure 10 for the increase of the Reynolds shear stress at $y < 0$ depending on the permeability.) This discussion supports the recent studies of Lee & Sung (2007), MacDonald *et al.* (2018) and Xu *et al.* (2021), which reported that non-k-type roughness was not automatically classified as the d-type roughness. Hence the increment of the dispersion part as the permeability at $w/k \simeq 1$ in figure 14 correlates to the transition from the d-type roughness to the k-type roughness. The above energy flow mechanism also explains why the studies by Stoyanova *et al.* (2019), Kim *et al.* (2020) and Shen *et al.* (2020) showed that the dispersion played a significant role in modifying turbulence.

4.4. *Characteristic roughness height*

To see the region up to where the roughness effects extend, figure 16 compares the streamwise r.m.s. velocity profiles. The smooth wall channel flow profiles at $Re_\tau = 395$ (Moser, Kim & Mansour 1999) and 550 (Hoyas & Jiménez 2008) are also compared. In any case, the difference between the present and smooth channel cases becomes evident

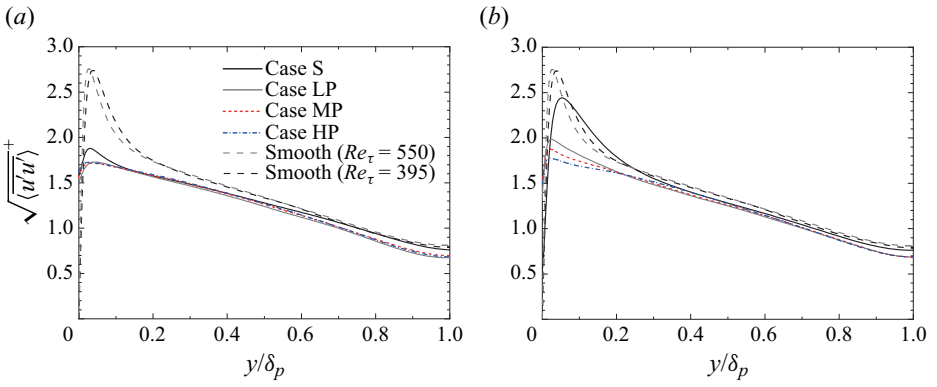

Figure 16. Streamwise r.m.s. velocity profiles against the wall-normal distance normalized by δ_p: (*a*) at $w/k \simeq 1$, (*b*) at $w/k \simeq 9$. The smooth wall channel data at $Re_\tau = 395$ and 550 are from Moser *et al.* (1999) and Hoyas & Jiménez (2008), respectively.

in the regions $y/\delta_p < 0.6$ and 0.3 for $w/k \simeq 1$ and 9, respectively. It is hence confirmed that the roughness effects extend up to those distances, which correspond approximately to $y = 4k$ and $2k$, respectively.

For the mean velocity profiles, we apply the logarithmic formula by Best (1935):

$$\frac{\langle U \rangle}{u_*} = \kappa^{-1} \ln \frac{y + d_0}{h_0}, \tag{4.10}$$

where d_0 and h_0 are the zero-plane displacement and a roughness scale. Usually, this has been applied to the flows over porous media and canopies (Nikora *et al.* 2002; Breugem *et al.* 2006; Nepf & Ghisalberti 2008; Suga *et al.* 2010; Manes *et al.* 2011). Using the fitting method described well in the literature (e.g. Breugem *et al.* 2006; Okazaki *et al.* 2022), the profiles are fitted to (4.10) for obtaining κ, d_0 and h_0, which are listed in table 2. Figures 17(*a*,*b*) show the presently fitted mean velocity profiles. Although there would be arguments against logarithmic fitting for relatively low Reynolds number flows, as shown in figures 17(*c*,*d*), the log-law indicator $\beta = (y + d_0)^+ \partial \langle U \rangle^+ / \partial y^+$ profiles show reasonably flat regions except for case S1. (For case LP, although the iteration number is reasonably large for obtaining the turbulence statistics, the plots suggest that it is not large enough for β. Hence we admit that the values for case LP obtained by the fitting contain certain errors.) We thus recognize that the flows in the present permeable cases have reasonable logarithmic velocity regions, except for case S1 in which a flat profile of β is not confirmed. Accordingly, we define the region below the log layer as the 'nominal' roughness sublayer, with its thickness δ_r as indicated graphically in figure 17(*c*). It is the distance between the zero-plane and the point where the β profile matches the horizontal flat line. Table 2 also lists the values of δ_r normalized by u_*. The nominal roughness sublayer thickness does not correspond to the thickness discussed with figure 16. In fact, $(\delta_r - d_0)/\delta_p = 0.03$–$0.11$. Moreover, when the zero-plane is considered for the origin of the boundary layer, the ratio of the nominal roughness sublayer to the boundary layer thickness is $\delta_r/(\delta_p + d_0) = 0.13$–$0.26$ in the present cases.

In permeable wall turbulence, κ is no longer constant, depending on the permeability as reported by Breugem *et al.* (2006), Suga *et al.* (2010) and Manes *et al.* (2011). Indeed, for $Re_b > 90\,000$, Manes *et al.* (2011) fitted their data with $\kappa = 0.32$. As shown in figure 18, although the experimental values of Okazaki *et al.* (2022) show a somewhat scattered

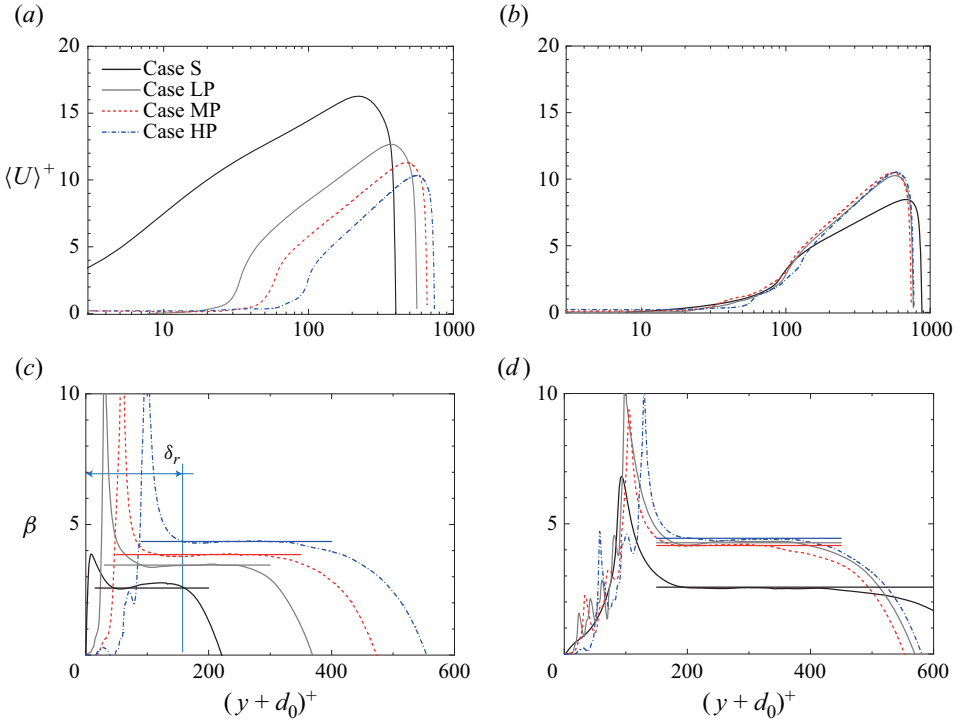

Figure 17. Streamwise plane-averaged mean velocity distributions in the semi-log scale and log-law indicator functions: (*a*) mean velocity profiles at $w/k \simeq 1$; (*b*) mean velocity profiles at $w/k \simeq 9$; (*c*) log-law indicator function β at $w/k \simeq 1$, with the graphical definition of the nominal roughness sublayer thickness δ_r; (*d*) log-law indicator function β at $w/k \simeq 9$. The solid thin horizontal lines in (*c*,*d*) correspond to $\beta = 1/\kappa$.

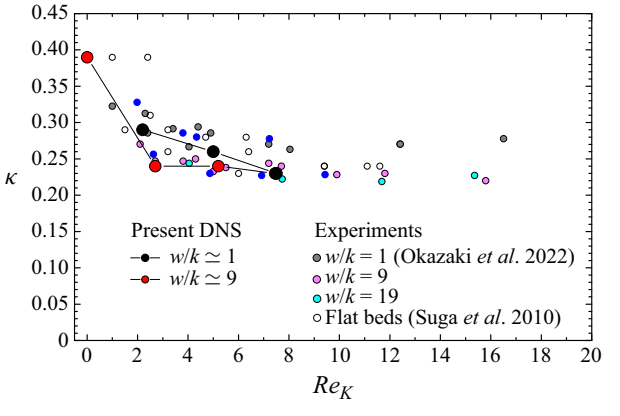

Figure 18. Variation of the von Kármán constant versus the permeability Reynolds number.

distribution, the plots distribute around the present results and one can see a general trend of κ depending on Re_K. Interestingly, although there may be w/k sensitivity, it looks less sensitive to w/k than the rib-bottom drag coefficient discussed with figure 13.

Another logarithmic formula of Nikuradse (1933) is, however, applied widely to discuss wall roughness. With the equivalent sand-grain roughness height k_s, it reads

$$\frac{\langle U\rangle}{u_*} = \kappa^{-1}\ln\frac{\hat{y}}{k_s} + 8.5, \tag{4.11}$$

where $\hat{y}$ is the wall-normal distance from the origin, which should be determined empirically (Jiménez 2004). Accordingly, in this study $\hat{y} = y + d_0$ is applied. (The scaling of d_0 was discussed extensively by Okazaki *et al.* (2022). They reported that although d_0 depended on both the rib spacing and the permeability, once the zero-plane displacement for the corresponding impermeable case d_s was given, $(d_0 - d_s)^+$ was scaled as $(d_0 - d_s)^+ \simeq 14Re_K$ or $(d_0 - d_s)^+ \simeq D_p^+$, where D_p^+ was the pore Reynolds number.) By coupling (4.10) and (4.11), we can re-fit the velocity data to Nikuradse's formula, and k_s can be rewritten with h_0 as $k_s = h_0\exp(8.5\kappa)$. However, we think that this process to estimate k_s is not a legitimately acceptable way to determine the equivalent sand-grain roughness height. We then call such a value the 'characteristic roughness height':

$$k_s^* = h_0\exp(8.5\kappa), \tag{4.12}$$

hereafter. Table 2 lists the obtained k_s^* normalized by u_*, and indicates that all cases are in the 'nominally' fully rough regime of $k_s^{*+} > 70$, except for case S1. Although the roughness function may be discussed, it is unsure how to determine the log-law shifts in this study due to the variation of the slant angle of the semi-logarithmic velocity profile, as seen in figure 17. Accordingly, this study focuses on k_s^* as a parameter for roughness effects. Note that although h_0 is another candidate for the parameter, since k_s^* includes explicitly the effects of h_0 and the non-constant κ by (4.12), we have found that k_s^* is a better scale to characterize permeable roughness, as discussed below.

Initially, we considered that δ_p might be a candidate to scale k_s^* at a higher Re_K since reasonable distributions of k_s^*/δ_p were seen in the present data. We have, however, found that it is not true by conducting an additional simulation of an open channel flow whose height corresponds to $\delta_p/k = 10$ for case MP9. This additional case is named MP9-OC, hereafter. The results indicate that since Re_τ is set to the same as that of case MP9, the obtained parameters do not change significantly from those of case MP9, although k_s^*/δ_p changes significantly. The parameters of case MP9-OC are $\kappa = 0.26$, $d_0^+ = 95$, $h_0^+ = 38$, $ks^{*+} = 346$ and $\delta_r^+ = 128$. They change slightly from the original values of case MP9 listed in table 2. Note that since the values of the parameters including the changing κ are slightly affected by δ_p/k (and hence H/k), the results indicate a certain limitation of the set-up adopted in this study.

Instead of δ_p, to discuss the permeability effect on k_s^*, we have found that the nominal roughness sublayer thickness δ_r is better than the viscous length scale for scaling k_s^*, as shown in figure 19. Indeed, we see that including the above additional result of case MP9-OC, k_s^* maintains a close relation with an inner layer parameter δ_r. It is seen that when Re_K becomes larger, asymptotically k_s^*/δ_r reaches approximately 2.5 for both $w/k \simeq 1$ and 9. Since the levels and characteristics of turbulence become quite similar in cases LP9, MP9, HP9 and HP1, we consider that the values of k_s^*/δ_r in those cases become similar. Experiments by Okazaki *et al.* (2022) support this trend for the higher Re_K cases, as seen in figure 19. When w/k becomes larger, as also indicated in figure 19, the experimental data by Okazaki *et al.* (2022) for $w/k = 19$ and the flat porous bed cases by Suga *et al.* (2010) also distribute around $k_s^*/\delta_r \simeq 2.5$ at $Re_K > 7$. Hence at a higher Re_K that is larger than 7, k_s^*/δ_r becomes independent of Re_K and looks almost constant around

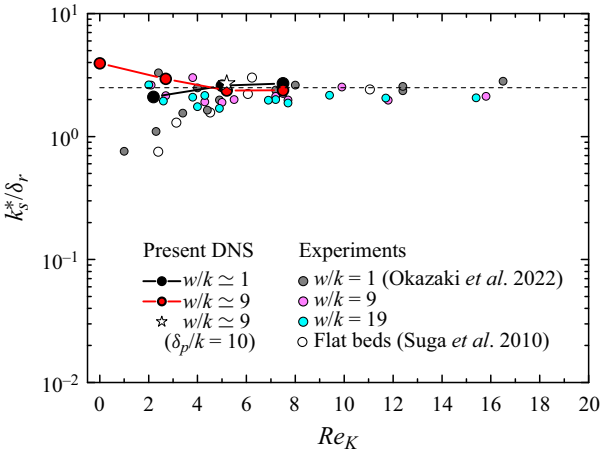

Figure 19. Characteristic roughness height versus the permeability Reynolds number. The star symbol is from the additional simulation with a higher channel height. The thin black dashed line indicates $k_s^*/\delta_r = 2.5$.

2.5 irrespective of the rib spacing, while in the transitional stage at $Re_K < 7$, k_s^*/δ_r varies depending on the cases. These trends suggest that some of the turbulence characteristics become insensitive to the surface topology at a high permeability Reynolds number. This is supported by the discussion of Voermans *et al.* (2017), who reported that many turbulence characteristics became independent of Re_K as it increased. White & Nepf (2007) also reported that the details of the porous layer were not important for the vortex structure once the inner layer instability was established.

4.5. *Premultiplied energy spectra*

To see the turbulence structures from spectrum spaces, figure 20 describes the one-dimensional premultiplied streamwise energy spectrum $(E_{uu,x}\kappa_x)^+$ distributions in the wall-normal direction. As for $w/k \simeq 1$, although the most energetic region is detached from the rib-top position at $y = 0$ in case S1, the levels of the energetic regions become lower, and the most energetic points look attached on the rib-top position ($y = 0$) in permeable cases. This corresponds to the profiles shown in figure 11(*a*). It is also seen that the energy with larger wavelengths propagates more toward the edge of the boundary layer, and the shapes of the contours tend to be square-like ones as the permeability increases. Notably, the most energetic wavelength in each case becomes slightly larger as the permeability increases. In case HP1, it becomes $\lambda_x/\delta_p \simeq 2$. As for $w/k \simeq 9$, the trends for the energy propagation and the most energetic wavelength are also observed, while in case HP9, the most energetic wavelength λ_x looks a little larger than $2\delta_p$. Furthermore, the outermost contours of cases HP1 and HP9 resemble each other, suggesting that some turbulence structures tend to be similar irrespective of the rib spacing when the permeability Reynolds number is high. This corresponds to the trends discussed in § 4.4 with figure 19.

Figure 21 shows two-dimensional premultiplied energy spectra $(E_{uu,xz}\kappa_x\kappa_z)^+$ for the x–z planes at $y/k = 0.5$. In the permeable cases, for both $w/k \simeq 1$ and 9, the most energetic point of $(E_{uu,xz}\kappa_x\kappa_z)^+$ is almost fixed at $\lambda_x/\delta_p \simeq 2$ in the streamwise direction, while in the region $\lambda_x/\delta_p > 2$, the contours tend to shift upwards in the spanwise direction as the permeability increases. This trend implies that some structures are expanded in the

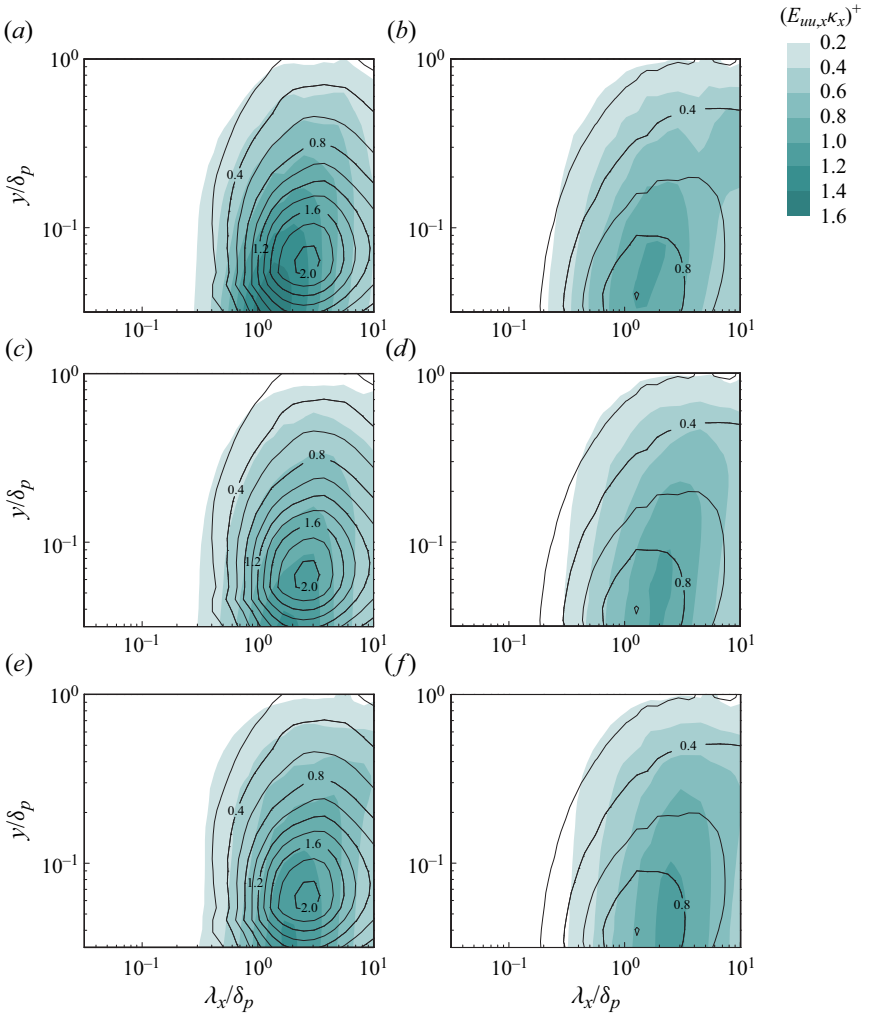

Figure 20. Premultiplied energy spectral distributions in the y-direction. The contours of $(E_{uu,x}\kappa_x)^+$ are plotted in the λ_x/δ_p–y/δ_p plane. The parameters κ_x and λ_x are the wavenumber and wavelength in the streamwise direction, respectively. The overlaid black lines in (*a*,*c*,*e*) and (*b*,*d*,*f*) are for cases S1 and S9, respectively. Plots are for (*a*) case LP1, (*b*) case LP9, (*c*) case MP1, (*d*) case MP9, (*e*) case HP1, (*f*) case HP9.

spanwise direction depending on the increase of the permeability, although it is not a clear evidence of the existence of spanwise rollers. Indeed, the roller structure cannot be confirmed in the two-point streamwise correlations shown in figure 5(*a*). Although the study by Kuwata & Suga (2016*b*) on turbulence over a flat porous bed observed spanwise rollers even at a relatively low $Re_K = 3.8$, once the surfaces are roughened, it may be considered that strong perturbations arising from the roughness elements disturb the development of such a structure. Spanwise rollers generated by the Kelvin–Helmholtz instability owing to velocity inflection may be appearing at much larger Reynolds numbers for the present flow configurations.

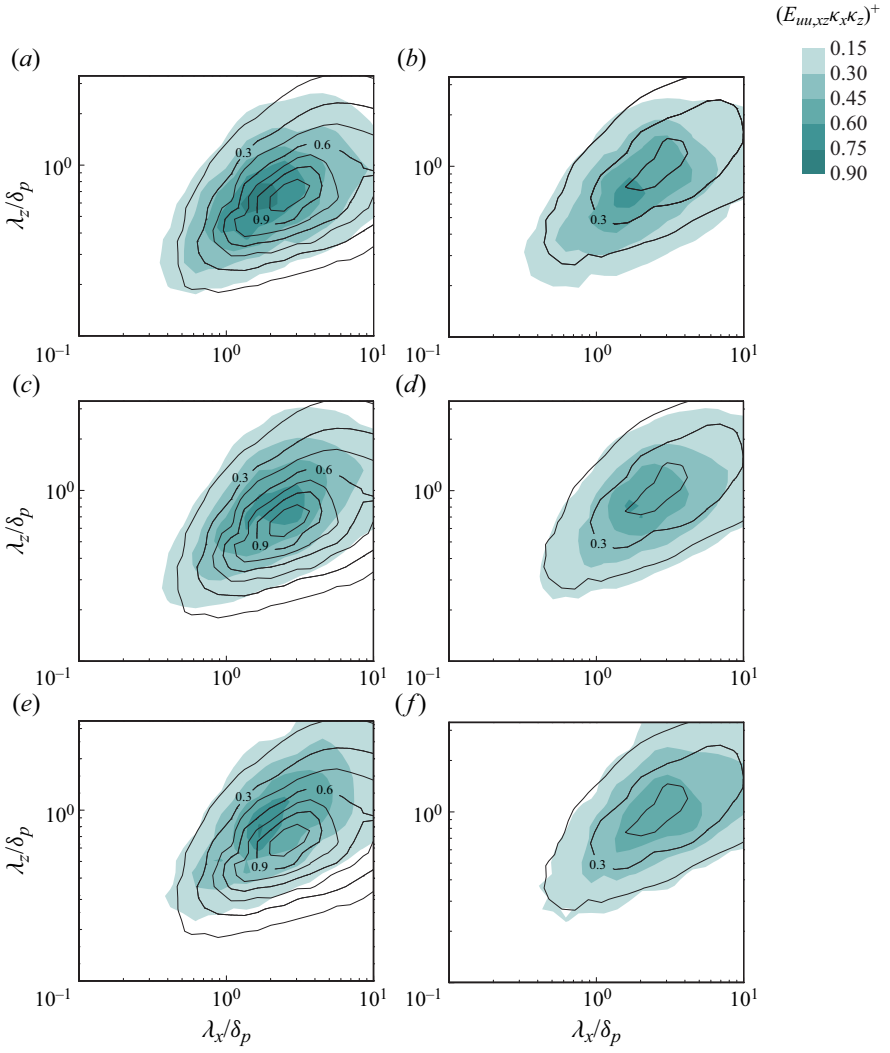

Figure 21. Two-dimensional premultiplied energy spectra for the streamwise–spanwise planes at $y/k = 0.5$. The contours of $(E_{uu,x}\kappa_x)^+$ are plotted in the λ_x/δ_p–λ_z/δ_p plane. The overlaid black lines in (*a*,*c*,*e*) and (*b*,*d*,*f*) are for cases S1 and S9, respectively. Plots are for (*a*) case LP1, (*b*) case LP9, (*c*) case MP1, (*d*) case MP9, (*e*) case HP1, (*f*) case HP9.

5. Conclusions

The effects of permeable roughness on turbulence have been described in the present study. Direct numerical simulations have been carried out for turbulent channel flows over porous rib-roughened porous layers at $Re_b = 5500$. Three types of foamed porous media are modelled by the Kelvin-cell structure with porosity 0.79 or 0.91. Their permeabilities are different, however, and the higher permeable case is designed to be the most permeable porous roughness consisting of the Kelvin cells. The higher permeable case is approximately one order more permeable than the lower permeable case. The simulated range of the permeability Reynolds number Re_K is 2.2–7.5 for the ratios of rib spacing to rib height $w/k \simeq 1$ and 9.

At $w/k \simeq 1$, as the permeability increases, while the magnitude of the Reynolds shear stress above the rib increases to a level comparable to that of $w/k \simeq 9$, it is significantly lower than that of $w/k \simeq 9$ at the porous layer surface. The magnitude of the dispersion stress inside the porous layer at $w/k \simeq 1$ is also significantly lower than that of $w/k \simeq 9$. These findings suggest that $w/k \simeq 9$ induces significantly larger surface mass transfer than $w/k \simeq 1$, depending on the permeability. The rib-bottom drag coefficient C_D, which includes the pressure drag and the frictional drag by the ribs, varies depending on both Re_K and the rib spacing, while it has each asymptotic limiting value for each rib spacing at the higher limit of Re_K. By integrating the double (time and space) averaged momentum equation, C_D is decomposed into laminar, rib-drag, dispersion and turbulence parts. From the analyses of the decomposed C_D and the budget equations for the double averaged fields, the mechanism for the increase of the turbulence quantities by the roughness effects and the transition from the d-type to k-type roughness at $w/k \simeq 1$, depending on the increase of Re_K, is elucidated. While the drag force, which has a direct relation to the roughness elements, is included in the momentum equation, it appears in the budget equation only for the streamwise dispersion stress. Accordingly, the roughness effects are transferred indirectly to the turbulence field through the mean shear and the dispersive shear production, which feeds the energy from the dispersion to turbulence fields. Since the mean shear in the rib region and the integrated dispersion part of C_D in the impermeable case at $w/k = 1$ are negligibly small, the roughness element effect on turbulence is very limited. As Re_K increases at $w/k \simeq 1$, however, since both the mean shear in the rib region and the integrated dispersion part increase, turbulence increases, reflecting the rib-roughness effects. This is the mechanism for the transition from the d-type to k-type roughness occurring at $w/k \simeq 1$, depending on Re_K. At $w/k \simeq 9$, since both the mean shear in the rib region and the integrated dispersion part of C_D are large enough, all the impermeable and permeable cases have significant rib-roughness effects. The indicated energy flow mechanism also explains why the dispersion played a significant role in modifying turbulence observed in the literature. Along with the data in the literature, it is suggested that the characteristic roughness height k_s^*, which is obtained by coupling Best's and Nikuradse's logarithmic velocity formulae, has an asymptotic limiting value $k_s^* \simeq 2.5\delta_r$ at $Re_K > 7$, irrespective of the rib spacing. Here, δ_r is the nominal roughness sublayer thickness. Consequently, the present study suggests that characteristics of turbulence over permeable roughness maintain evident inner layer effects even in the cases where the rib effects become unimportant at a higher Re_K.

From the one-dimensional premultiplied streamwise energy spectrum distributions in the wall-normal direction, it is suggested that the turbulence structures become large towards the edge of the equivalent boundary layer thickness δ_p, and tend to be similar irrespective of the rib spacing when Re_K becomes large. The two-dimensional premultiplied energy spectra for the streamwise–spanwise planes imply that some structures are expanded in the spanwise direction depending on the increase of the permeability, while spanwise rollers are not yet formed in the range of the present Re_K. Although previously we observed spanwise rollers even at a relatively low Re_K in turbulence over a flat porous bed, once the surfaces are roughened, it is considered that strong perturbations arising from the roughness elements disturb the development of the spanwise roller structure originated by the inflection point instability.

Acknowledgements. The authors express their gratitude to Y. Nishiyama and K. Nishino for their collaboration to initiate the present research project.

Funding. A part of this study was supported financially by research grant no. 19H02069 of the JSPS. The numerical calculations were carried out on the TSUBAME3.0 supercomputer at the Tokyo Institute of Technology in research projects hp190013 and hp200066 supported by the High Performance Computing Infrastructure (HPCI) of the Research Organization for Information Science and Technology (RiST), Japan.

Declaration of interests. The authors report no conflict of interest.

Author ORCIDs.
Kazuhiko Suga https://orcid.org/0000-0001-9313-1816;
Yusuke Kuwata https://orcid.org/0000-0002-9489-2788.

Appendix A. Parameters for the D3Q27 multiple-relaxation-time lattice Boltzmann method

For the D3Q27 model by Suga *et al.* (2015), the components of the discrete velocity vector are

$$\begin{aligned}&\left({}^{\mathrm{T}}\boldsymbol{\xi}_0\,{}^{\mathrm{T}}\boldsymbol{\xi}_1\,{}^{\mathrm{T}}\boldsymbol{\xi}_2\,{}^{\mathrm{T}}\boldsymbol{\xi}_3\cdots{}^{\mathrm{T}}\boldsymbol{\xi}_{25}\,{}^{\mathrm{T}}\boldsymbol{\xi}_{26}\right)\\ &\quad= c\begin{pmatrix}0&1&0&-1&0&0&0&1&-1&-1&1&1&0&-1&0&1\\0&0&1&0&-1&0&0&1&1&-1&-1&0&1&0&-1&0\\0&0&0&0&0&1&-1&0&0&0&0&1&1&1&1&-1\\ 0&-1&0&1&-1&-1&1&1&-1&-1&1\\1&0&-1&1&1&-1&-1&1&1&-1&-1\\-1&-1&-1&1&1&1&1&-1&-1&-1&-1\end{pmatrix},\end{aligned}\tag{A1}$$

where the lattice velocity c is defined as $c = \Delta/\delta t$, Δ being the lattice spacing. The sound speed is $c_s = c/\sqrt{3}$, and the weighting parameter w_α is

$$w_\alpha = \begin{cases}8/27 & (\alpha = 0),\\ 2/27 & (\alpha = 1,\ldots,6),\\ 1/54 & (\alpha = 7,\ldots,18),\\ 1/216 & (\alpha = 19,\ldots,26).\end{cases}\tag{A2}$$

The collision matrix $\hat{\boldsymbol{S}}$ is diagonal,

$$\begin{aligned}\hat{\boldsymbol{S}} \equiv \mathrm{diag}(&0,0,0,0,s_4,s_5,s_5,s_7,s_7,s_7,s_{10},s_{10},s_{10},\\ &s_{13},s_{13},s_{13},s_{16},s_{17},s_{18},s_{18},s_{20},s_{20},s_{20},s_{23},s_{23},s_{23},s_{26}),\end{aligned}\tag{A3}$$

and the relaxation parameters slightly modified by Kuwata & Suga (2021) are

$$\begin{aligned}&s_4 = 1.54,\ s_7 = s_5,\ s_{10} = 1.96,\ s_{13} = 1.83,\ s_{16} = 1.4,\\ &s_{17} = 1.61,\ s_{18} = s_{20} = 1.98,\ s_{23} = s_{26} = 1.74,\end{aligned}\tag{A4}$$

where s_5 is related to the kinematic viscosity ν as

$$\nu = c_s^2\left(\frac{1}{s_5} - \frac{1}{2}\right)\delta t.\tag{A5}$$

The corresponding 27×27 transformation matrix is

$$\boldsymbol{M} = \begin{pmatrix}
1 & 1 & 1 & 1 & 1 & 1 & 1 & 1 & 1 & 1 & 1 & 1 & 1 & 1 & 1 \\
0 & 1 & 0 & -1 & 0 & 0 & 0 & 1 & -1 & -1 & 1 & 1 & 0 & -1 & 0 \\
0 & 0 & 1 & 0 & -1 & 0 & 0 & 1 & 1 & -1 & -1 & 0 & 1 & 0 & -1 \\
0 & 0 & 0 & 0 & 0 & 1 & -1 & 0 & 0 & 0 & 0 & 1 & 1 & 1 & 1 \\
-2 & -1 & -1 & -1 & -1 & -1 & -1 & 0 & 0 & 0 & 0 & 0 & 0 & 0 & 0 \\
0 & 2 & -1 & 2 & -1 & -1 & -1 & 1 & 1 & 1 & 1 & 1 & -2 & 1 & -2 \\
0 & 0 & 1 & 0 & 1 & -1 & -1 & 1 & 1 & 1 & 1 & -1 & 0 & -1 & 0 \\
0 & 0 & 0 & 0 & 0 & 0 & 0 & 1 & -1 & 1 & -1 & 0 & 0 & 0 & 0 \\
0 & 0 & 0 & 0 & 0 & 0 & 0 & 0 & 0 & 0 & 0 & 0 & 1 & 0 & -1 \\
0 & 0 & 0 & 0 & 0 & 0 & 0 & 0 & 0 & 0 & 0 & 1 & 0 & -1 & 0 \\
0 & -4 & 0 & 4 & 0 & 0 & 0 & -1 & 1 & 1 & -1 & -1 & 0 & 1 & 0 \\
0 & 0 & -4 & 0 & 4 & 0 & 0 & -1 & -1 & 1 & 1 & 0 & -1 & 0 & 1 \\
0 & 0 & 0 & 0 & 0 & -4 & 4 & 0 & 0 & 0 & 0 & -1 & -1 & -1 & -1 \\
0 & 4 & 0 & -4 & 0 & 0 & 0 & -2 & 2 & 2 & -2 & -2 & 0 & 2 & 0 \\
0 & 0 & 4 & 0 & -4 & 0 & 0 & -2 & -2 & 2 & 2 & 0 & -2 & 0 & 2 \\
0 & 0 & 0 & 0 & 0 & 4 & -4 & 0 & 0 & 0 & 0 & -2 & -2 & -2 & -2 \\
4 & 0 & 0 & 0 & 0 & 0 & 0 & -1 & -1 & -1 & -1 & -1 & -1 & -1 & -1 \\
-8 & 4 & 4 & 4 & 4 & 4 & 4 & -2 & -2 & -2 & -2 & -2 & -2 & -2 & -2 \\
0 & -4 & 2 & -4 & 2 & 2 & 2 & 1 & 1 & 1 & 1 & 1 & -2 & 1 & -2 \\
0 & 0 & -2 & 0 & -2 & 2 & 2 & 1 & 1 & 1 & 1 & -1 & 0 & -1 & 0 \\
0 & 0 & 0 & 0 & 0 & 0 & 0 & -2 & 2 & -2 & 2 & 0 & 0 & 0 & 0 \\
0 & 0 & 0 & 0 & 0 & 0 & 0 & 0 & 0 & 0 & 0 & 0 & -2 & 0 & 2 \\
0 & 0 & 0 & 0 & 0 & 0 & 0 & 0 & 0 & 0 & 0 & -2 & 0 & 2 & 0 \\
0 & 0 & 0 & 0 & 0 & 0 & 0 & 1 & -1 & -1 & 1 & -1 & 0 & 1 & 0 \\
0 & 0 & 0 & 0 & 0 & 0 & 0 & -1 & -1 & 1 & 1 & 0 & 1 & 0 & -1 \\
0 & 0 & 0 & 0 & 0 & 0 & 0 & 0 & 0 & 0 & 0 & 1 & -1 & 1 & -1 \\
0 & 0 & 0 & 0 & 0 & 0 & 0 & 0 & 0 & 0 & 0 & 0 & 0 & 0 & 0
\end{pmatrix}$$

$$\begin{pmatrix}
1 & 1 & 1 & 1 & 1 & 1 & 1 & 1 & 1 & 1 & 1 & 1 \\
1 & 0 & -1 & 0 & 1 & -1 & -1 & 1 & 1 & -1 & -1 & 1 \\
0 & 1 & 0 & -1 & 1 & 1 & -1 & -1 & 1 & 1 & -1 & -1 \\
-1 & -1 & -1 & -1 & 1 & 1 & 1 & 1 & -1 & -1 & -1 & -1 \\
0 & 0 & 0 & 0 & 1 & 1 & 1 & 1 & 1 & 1 & 1 & 1 \\
1 & -2 & 1 & -2 & 0 & 0 & 0 & 0 & 0 & 0 & 0 & 0 \\
-1 & 0 & -1 & 0 & 0 & 0 & 0 & 0 & 0 & 0 & 0 & 0 \\
0 & 0 & 0 & 0 & 1 & -1 & 1 & -1 & 1 & -1 & 1 & -1 \\
0 & -1 & 0 & 1 & 1 & 1 & -1 & -1 & -1 & -1 & 1 & 1 \\
-1 & 0 & 1 & 0 & 1 & -1 & -1 & 1 & -1 & 1 & 1 & -1 \\
-1 & 0 & 1 & 0 & 2 & -2 & -2 & 2 & 2 & -2 & -2 & 2 \\
0 & -1 & 0 & 1 & 2 & 2 & -2 & -2 & 2 & 2 & -2 & -2 \\
1 & 1 & 1 & 1 & 2 & 2 & 2 & 2 & -2 & -2 & -2 & -2 \\
-2 & 0 & 2 & 0 & 1 & -1 & -1 & 1 & 1 & -1 & -1 & 1 \\
0 & -2 & 0 & 2 & 1 & 1 & -1 & -1 & 1 & 1 & -1 & -1 \\
2 & 2 & 2 & 2 & 1 & 1 & 1 & 1 & -1 & -1 & -1 & -1 \\
-1 & -1 & -1 & -1 & 1 & 1 & 1 & 1 & 1 & 1 & 1 & 1 \\
-2 & -2 & -2 & -2 & 1 & 1 & 1 & 1 & 1 & 1 & 1 & 1 \\
1 & -2 & 1 & -2 & 0 & 0 & 0 & 0 & 0 & 0 & 0 & 0 \\
-1 & 0 & -1 & 0 & 0 & 0 & 0 & 0 & 0 & 0 & 0 & 0 \\
0 & 0 & 0 & 0 & 1 & -1 & 1 & -1 & 1 & -1 & 1 & -1 \\
0 & 2 & 0 & -2 & 1 & 1 & -1 & -1 & -1 & -1 & 1 & 1 \\
2 & 0 & -2 & 0 & 1 & -1 & -1 & 1 & -1 & 1 & 1 & -1 \\
-1 & 0 & 1 & 0 & 0 & 0 & 0 & 0 & 0 & 0 & 0 & 0 \\
0 & 1 & 0 & -1 & 0 & 0 & 0 & 0 & 0 & 0 & 0 & 0 \\
-1 & 1 & -1 & 1 & 0 & 0 & 0 & 0 & 0 & 0 & 0 & 0 \\
0 & 0 & 0 & 0 & 1 & -1 & 1 & -1 & -1 & 1 & -1 & 1
\end{pmatrix} \tag{A6}$$

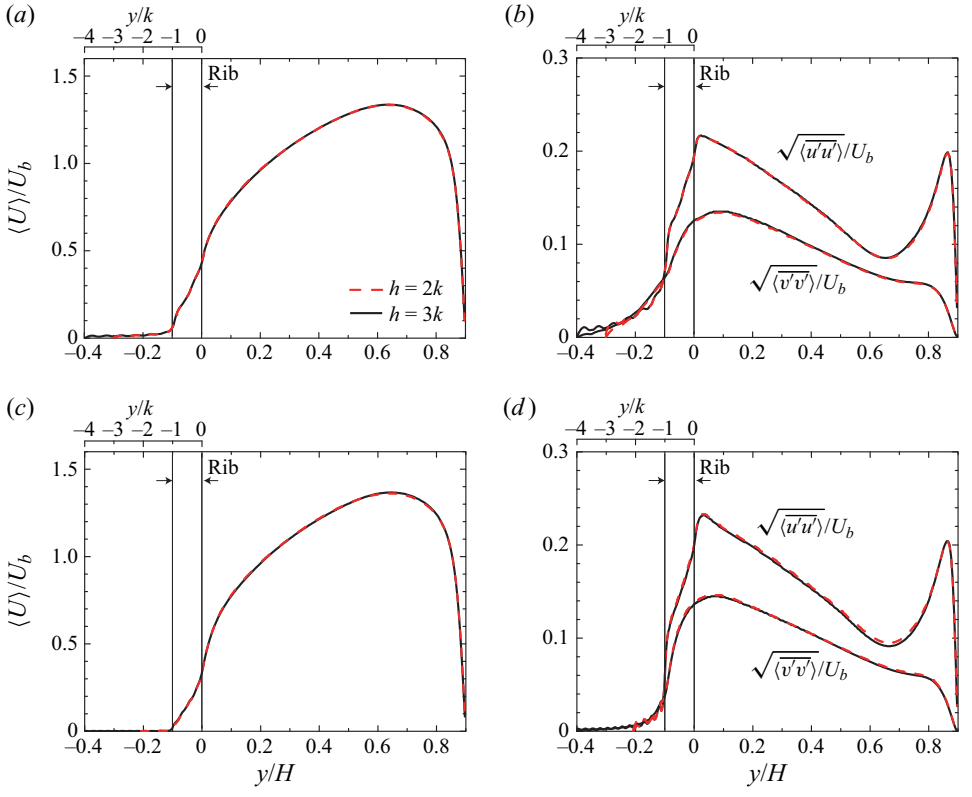

Figure 22. Effects of the thickness of the porous layer: (*a*) comparison of the mean velocity profiles in case HP9; (*b*) comparison of the r.m.s. velocity profiles in case HP9; (*c*) comparison of the mean velocity profiles in case LP9; (*d*) comparison of the r.m.s. velocity profiles in case LP9. The solid black curves correspond to $h = 3k$, while the red dash curves in (*a*,*b*) and (*c*,*d*) correspond to $h = 2k$ and $h = k$, respectively.

Appendix B. Validation of the porous layer thickness

The thickness effect of the presently applied porous layer on turbulence is examined by comparing the results with those by different thickness. Figures 22(*a*,*b*) compare the results by $h = 2k$ and $h = 3k$ for case HP9. Figures 22(*c*,*d*) compare the results by $h = k$ and $h = 3k$ for case LP9. For the mean velocities and the r.m.s. velocities, since the profiles of the two different thickness cases almost perfectly overlap each other, we confirm that the presently applied thicknesses $h = 3k$ and $h = k$ for cases HP and LP, respectively, are thick enough to discuss turbulence over porous rib-roughened beds. Since the difference between cases HP and MP is only the ligament diameter d, the confirmation with case HP also confirms the validity for case MP.

Appendix C. Decomposition of the drag coefficient

When $\eta \le \delta_p$, integration of (4.5) from η to δ_p gives

$$0 = -\frac{1}{\rho}\frac{\partial \langle \bar{p} \rangle^f}{\partial x}\int_\eta^{\delta_p} \epsilon \,\mathrm{d}y \underbrace{- \nu \left.\frac{\partial \epsilon \langle \bar{u} \rangle^f}{\partial y}\right|_\eta + (R_{12}(\eta) + T_{12}(\eta))}_{=-\tau_{(\eta)}} - \int_\eta^{\delta_p} \bar{f}_1 \,\mathrm{d}y, \tag{C1}$$

since $\tau_{(\delta_p)} = 0$. This form can be rewritten as

$$-\frac{1}{\rho}\frac{\partial \langle \bar{p} \rangle^f}{\partial x}\left(-\int_{-k}^{\eta} \epsilon \,\mathrm{d}y + \int_{-k}^{\delta_p} \epsilon \,\mathrm{d}y\right) = \tau_{(\eta)} + \int_{\eta}^{\delta_p} \bar{f}_1 \,\mathrm{d}y. \tag{C2}$$

From (4.5), the drag at the rib-bottom position $y = -k$ balances with the pressure gradient as

$$\tau_b = -\frac{\partial \langle \bar{p} \rangle^f}{\partial x}\int_{-k}^{\delta_p} \epsilon \,\mathrm{d}y. \tag{C3}$$

Accordingly, since $C_D = 2\tau_b/(\rho U_b^2)$, (C2) may be rewritten as

$$C_D\left(1 - \frac{\int_{-k}^{\eta} \epsilon \,\mathrm{d}y}{\int_{-k}^{\delta_p} \epsilon \,\mathrm{d}y}\right) = \frac{2}{U_b^2}\left(\tau_{(\eta)} + \int_{\eta}^{\delta_p} \bar{f}_1 \,\mathrm{d}y\right). \tag{C4}$$

When $\epsilon \langle \bar{u} \rangle^f|_{(-k)}$ is assumed to be ignorably small, integration of (C4) by η between $-k$ and y gives

$$C_D\int_{-k}^{y}\left(1 - \frac{\int_{-k}^{\eta} \epsilon \,\mathrm{d}y}{\int_{-k}^{\delta_p} \epsilon \,\mathrm{d}y}\right)\mathrm{d}\eta = \frac{2\nu}{U_b^2}\epsilon \langle \bar{u} \rangle^f + \frac{2}{U_b^2}\int_{-k}^{y}\left(\int_{\eta}^{\delta_p} \bar{f}_1 \,\mathrm{d}y - R_{12} - T_{12}\right)\mathrm{d}\eta. \tag{C5}$$

By integrating further by y between $-k$ and $H - k$, we obtain

$$\begin{aligned} &C_D\int_{-k}^{H-k}\int_{-k}^{y}\left(1 - \frac{\int_{-k}^{\eta} \epsilon \,\mathrm{d}y}{\int_{-k}^{\delta_p} \epsilon \,\mathrm{d}y}\right)\mathrm{d}\eta \,\mathrm{d}y \\ &\quad = \frac{2\nu}{U_b^2}\int_{-k}^{H-k} \epsilon \langle \bar{u} \rangle^f \,\mathrm{d}y + \frac{2}{U_b^2}\int_{-k}^{H-k}\int_{-k}^{y}\left(\int_{\eta}^{\delta_p} \bar{f}_1 \,\mathrm{d}y - R_{12} - T_{12}\right)\mathrm{d}\eta \,\mathrm{d}y. \end{aligned} \tag{C6}$$

Here, when Ψ is defined as

$$\Psi = \left\{\frac{1}{2H^2}\int_{-k}^{H-k}\int_{-k}^{y}\left(1 - \frac{\int_{-k}^{\eta} \epsilon \,\mathrm{d}y}{\int_{-k}^{\delta_p} \epsilon \,\mathrm{d}y}\right)\mathrm{d}\eta \,\mathrm{d}y\right\}^{-1}, \tag{C7}$$

since $\int_{-k}^{H-k} \epsilon \langle \bar{u} \rangle^f \,\mathrm{d}y = U_b$, (C6) can be rewritten as

$$\begin{aligned} C_D = \Psi\Bigg[&\frac{1}{Re_b} + \frac{1}{U_b^2H^2}\int_{-k}^{H-k}\int_{-k}^{y}\int_{\eta}^{\delta_p} \bar{f}_1 \,\mathrm{d}y \,\mathrm{d}\eta \,\mathrm{d}y \\ &+ \frac{1}{U_b^2H^2}\int_{-k}^{H-k}\int_{-k}^{y}(-R_{12})\,\mathrm{d}\eta \,\mathrm{d}y + \frac{1}{U_b^2H^2}\int_{-k}^{H-k}\int_{-k}^{y}(-T_{12})\,\mathrm{d}\eta \,\mathrm{d}y\Bigg]. \end{aligned} \tag{C8}$$

When the double and triple integrations are transformed into single integrations as in (C9) below, we can obtain (4.6) and (4.7) with $f_x = 0$ at $y \geq 0$.

When $\mathbb{R}_{12}(y) = \int_{-k}^{y} R_{12}(\eta)\,\mathrm{d}\eta$, its differentiation is $\mathbb{R}'_{12}(y) = R_{12}(y)$. Then the double integration is transformed into a single integration as

$$\begin{aligned}\int_{-k}^{H-k} \mathbb{R}_{12}\,\mathrm{d}y &= \left[y\mathbb{R}_{12}\right]_{-k}^{H-k} - \int_{-k}^{H-k} y\mathbb{R}'_{12}\,\mathrm{d}y \\ &= (H-k)\int_{-k}^{H-k} R_{12}\,\mathrm{d}y + k\int_{-k}^{-k} R_{12}\,\mathrm{d}y - \int_{-k}^{H-k} yR_{12}\,\mathrm{d}y \\ &= \int_{-k}^{H-k} (H-k-y)R_{12}\,\mathrm{d}y. \end{aligned} \tag{C9}$$

Triple integrations also can be transformed into single integrations by repeating the above transformation.

References

Ashrafian, A., Andersson, H. & Manhart, M. 2004 DNS of turbulent flow in a rod-roughened channel. *Intl J. Heat Fluid Flow* **25**, 373–383.

Bespalko, D., Pollard, A. & Uddin, M. 2012 Analysis of the pressure fluctuations from an LBM simulation of turbulent channel flow. *Comput. Fluids* **54**, 143–146.

Best, A.C. 1935 Transfer of heat and momentum in lowest layers of the atmosphere. *Tech. Rep.* 65. Geophys. Mem. Met Office.

Breugem, W.P., Boersma, B.J. & Uittenbogaard, R.E. 2006 The influence of wall permeability on turbulent channel flow. *J. Fluid Mech.* **562**, 35–72.

Burattini, P., Leonardi, S., Orlandi, P. & Antonia, R.A. 2008 Comparison between experiments and direct numerical simulations in a channel flow with roughness on one wall. *J. Fluid Mech.* **600**, 403–426.

Chikatamarla, S.S., Frouzakis, C.E., Karlin, I.V., Tomboulides, A.G. & Boulouchos, K.B. 2010 Lattice Boltzmann method for direct numerical simulation of turbulent flows. *J. Fluid Mech.* **656**, 298–308.

Chukwudozie, C. & Tyagi, M. 2013 Pore scale inertial flow simulations in 3-D smooth and rough sphere packs using lattice Boltzmann method. *AIChE J.* **59** (12), 247–259.

Chun, B. & Ladd, A.J. 2007 Interpolated boundary condition for lattice Boltzmann simulations of flows in narrow gaps. *Phys. Rev.* E **75**, 066705.

Chung, D., Hutchins, N., Schultz, M.P. & Flack, K.A. 2021 Predicting the drag of rough surfaces. *Annu. Rev. Fluid Mech.* **53** (1), 439–471.

Coceal, O., Dobre, A., Thomas, T.G. & Belcher, S.E. 2007 Structure of turbulent flow over regular arrays of cubical roughness. *J. Fluid Mech.* **589**, 375–409.

Cui, J., Patel, V.C. & Lin, C.-L. 2003 Large-eddy simulation of turbulent flow in a channel with rib roughness. *Intl J. Heat Fluid Flow* **24**, 372–388.

d'Humières, D., Ginzburg, I., Krafczyk, M., Lallemand, P. & Luo, L.-S. 2002 Multiple-relaxation-time lattice Boltzmann models in three dimensions. *Phil. Trans. R. Soc. Lond.* A **360** (1792), 437–451.

Efstathiou, C. & Luhar, M. 2018 Mean turbulence statistics in boundary layers over high-porosity foams. *J. Fluid Mech.* **841**, 351–379.

Fattahi, E., Waluga, C., Wohlmuth, B., Rü de, U., Manhart, M. & Helmig, R. 2016 Lattice Boltzmann methods in porous media simulations: from laminar to turbulent flow. *Comput. Fluids* **140**, 247–259.

Feng, S., Li, F., Zhang, F. & Lu, T.J. 2018 Natural convection in metal foam heat sinks with open slots. *Expl Therm. Fluid Sci.* **91**, 354–362.

Finnigan, J. 2000 Turbulence in plant canopies. *Annu. Rev. Fluid Mech.* **32**, 519–571.

Flack, K.A. & Schultz, M.P. 2014 Roughness effects on wall-bounded turbulent flows. *Phys. Fluids* **26**, 1013051.

Fukagata, K., Iwamoto, K. & Kasagi, N. 2002 Contribution of Reynolds stress distribution to the skin friction in wall-bounded flows. *Phys. Fluids* **14**, L73–L76.

Gómez-de Segura, G. & García-Mayoral, R. 2019 Turbulent drag reduction by anisotropic permeable substrates – analysis and direct numerical simulations. *J. Fluid Mech.* **875**, 124–172.

HANJALIĆ, K. & LAUNDER, B.E. 1972 Fully developed asymmetric flow in a plane channel. *J. Fluid Mech.* **51**, 301–335.

HE, X. & LUO, L.-S. 1997 Lattice Boltzmann model for the incompressible Navier–Stokes equation. *J. Stat. Phys.* **88** (3/4), 927–944.

HOLDYCH, D.J., NOBLE, D.R., GEORGIADIS, J.G. & BUCKIUS, R.O. 2004 Truncation error analysis of lattice Boltzmann methods. *J. Comput. Phys.* **193** (2), 595–619.

HOYAS, S. & JIMÉNEZ, J. 2008 Reynolds number effects on the Reynolds stress budgets in turbulent channels. *Phys. Fluids* **20**, 101511.

IACOVIDES, H. & RAISEE, M. 1999 Recent progress in the computation of flow and heat transfer in internal cooling passages of turbine blades. *Intl J. Heat Fluid Flow* **20**, 320–328.

JARVELA, J. 2005 Effect of submerged flexible vegetation on flow structure and resistance. *J. Hydrol.* **307**, 233–241.

JIMÉNEZ, J. 2004 Turbulent flows over rough walls. *Annu. Rev. Fluid Mech.* **36** (1), 173–196.

KIM, T., BLOIS, G. & CHRISTENSEN, K. 2020 Experimental evidence of amplitude modulation in permeable-wall turbulence. *J. Fluid Mech.* **887**, A3.

KUMAR, P. & TOPIN, F. 2017 State-of-the-art of pressure drop in open-cell porous foams: review of experiments and correlations. *Trans. ASME J. Fluids Engng* **139**, 111401.

KUWATA, Y. & SUGA, K. 2013 Modelling turbulence around and inside porous media based on the second moment closure. *Intl J. Heat Fluid Flow* **43**, 35–51.

KUWATA, Y. & SUGA, K. 2015 Progress in the extension of a second-moment closure for turbulent environmental flows. *Intl J. Heat Fluid Flow* **51**, 268–284.

KUWATA, Y. & SUGA, K. 2016*a* Imbalance-correction grid-refinement method for lattice Boltzmann flow simulations. *J. Comput. Phys.* **311**, 348–362.

KUWATA, Y. & SUGA, K. 2016*b* Lattice Boltzmann direct numerical simulation of interface turbulence over porous and rough walls. *Intl J. Heat Fluid Flow* **61**, 145–157.

KUWATA, Y. & SUGA, K. 2017 Direct numerical simulation of turbulence over anisotropic porous media. *J. Fluid Mech.* **831**, 41–71.

KUWATA, Y. & SUGA, K. 2021 Wall-modeled large eddy simulation of turbulent heat transfer by the lattice Boltzmann method. *J. Comput. Phys.* **433**, 110186.

KUWATA, Y., SUGA, K. & SAKURAI, Y. 2014 Development and application of a multi-scale k-ε model for turbulent porous medium flows. *Intl J. Heat Fluid Flow* **49**, 135–150.

LEE, S.-H. & SUNG, H.J. 2007 Direct numerical simulation of the turbulent boundary layer over a rod-roughened wall. *J. Fluid Mech.* **584**, 125–146.

LEONARDI, S., ORLANDI, P., DJENIDI, L. & ANTONIA, R.A. 2004 Structure of turbulent channel flow with square bars on one wall. *Intl J. Heat Fluid Flow* **25** (3), 384–392.

LEONARDI, S., ORLANDI, P., SMALLEY, R.J., DJENIDI, L. & ANTONIA, R.A. 2003 Direct numerical simulations of turbulent channel flow with transverse square bars on one wall. *J. Fluid Mech.* **491**, 229–238.

LOVERA, F. & KENNEDY, J.F. 1969 Friction factors for flat bed flows in sand channels. *J. Hydraul. Div. ASCE* **95**, 1227–1234.

MACDONALD, M., OOI, A., GARCÍA-MAYORAL, R., HUTCHINS, N. & CHUNG, D. 2018 Direct numerical simulation of high aspect ratio spanwise-aligned bars. *J. Fluid Mech.* **843**, 126–155.

MANES, C., POGGI, D. & RIDOL, L. 2011 Turbulent boundary layers over permeable walls: scaling and near-wall structure. *J. Fluid Mech.* **687**, 141–170.

MANES, C., POKRAJAC, D., MCEWAN, I. & NIKORA, V. 2009 Turbulence structure of open channel flows over permeable and impermeable beds: a comparative study. *Phys. Fluids* **21** (12), 125109.

MOSER, R.D., KIM, J. & MANSOUR, N.N. 1999 Direct numerical simulation of turbulent channel flow up to $Re_\tau = 590$. *Phys. Fluids* **11**, 943–945.

NAGANO, Y., HATTORI, H. & HOURA, T. 2004 DNS of velocity and thermal fields in turbulent channel flow with transverse-rib roughness. *Intl J. Heat Fluid Flow* **25** (3), 393–403.

NAKAGAWA, H., TSUJIMOTO, T. & SHIMIZU, Y. 1991 Turbulent flow with small relative submergence. In *Fluvial Hydraulics of Mountain Regions* (ed. A. Armanini & G. Di Silvio), Lecture Notes in Earth Sciences, vol. 37, pp. 33–44. Springer.

NEPF, H. & GHISALBERTI, M. 2008 Flow and transport in channels with submerged vegetation. *Acta Geophys.* **56**, 753–777.

NIKORA, V., KOLL, K., MCLEAN, S., DITTRICH, A. & ABERLE, J. 2002 Zero-plane displacement for rough-bed open-channel flows. In *Int. Conf. Fluvial Hydraulics River Flow 2002, Louvain-la-Neuve, Belgium* (ed. Y. Zech & D. Bousmar), pp. 83–92. Balkema.

NIKURADSE, J. 1933 Strömungsgesetze in rauhen rohren. *VDI-Forsch.* **361**.

OKAZAKI, Y., SHIMIZU, A., KUWATA, Y. & SUGA, K. 2020 Turbulence characteristics over k-type rib roughened porous walls. *Intl J. Heat Fluid Flow* **82**, 108541.

OKAZAKI, Y., TAKASE, Y., KUWATA, Y. & SUGA, K. 2021 Describing characteristic parameters of turbulence over two-dimensional porous roughness. *J. Therm. Sci. Technol.* **16**, JTST0027.

OKAZAKI, Y., TAKASE, Y., KUWATA, Y. & SUGA, K. 2022 Turbulent channel flows over porous rib-roughed walls. *Exp. Fluids* **63**, 66.

ORLANDI, P., SASSUN, D. & LEONARDI, S. 2016 DNS of conjugate heat transfer in presence of rough surfaces. *Intl J. Heat Mass Transfer* **100**, 250–266.

PADHI, E., PENNA, N., DEY, S. & GAUDIO, R. 2018 Hydrodynamics of water-worked and screeded gravel beds: a comparative study. *Phys. Fluids* **30**, 085105.

PAN, C., LUO, L.-S. & MILLER, C.T. 2006 An evaluation of lattice Boltzmann schemes for porous medium flow simulation. *Comput. Fluids* **35**, 957–965.

PERRY, A.E., SCHOFIELD, W.H. & JOUBERT, P.N. 1969 Rough wall turbulent boundary layers. *J. Fluid Mech.* **37**, 383–413.

PIOMELLI, U. 2019 Recent advances in the numerical simulation of rough-wall boundary layers. *Phys. Chem. Earth* **113**, 63–72.

POGGI, D., PORPORATO, A., RIDOLFI, L., ALBERTSON, J.D. & KATUL, G.G. 2004 The effect of vegetation density on canopy sub-layer turbulence. *Boundary-Layer Meteorol.* **111** (3), 565–587.

POKRAJAC, D., FINNIGAN, J.J., MANES, C., MCEWAN, I. & NIKORA, V. 2006 On the definition of the shear velocity in rough bed open channel flows. In *River Flow 2006* (ed. R.M.L. Ferreira, E.C.T.L. Alves, J.G.A.B. Leal & A.H. Cardoso), pp. 89–98. Taylor & Francis.

POKRAJAC, D. & MANES, C. 2009 Velocity measurements of a free-surface turbulent flow penetrating a porous medium composed of uniform-size spheres. *Transp. Porous Med.* **78**, 367–383.

RAUPACH, M.R., ANTONIA, R.A. & RAJAGOPALAN, S. 1991 Rough-wall turbulent boundary layers. *Appl. Mech. Rev.* **44**, 1–25.

ROSTI, M.E., BRANDT, L. & PINELLI, A. 2018 Turbulent channel flow over an anisotropic porous wall – drag increase and reduction. *J. Fluid Mech.* **842**, 381–394.

SHEN, G., YUAN, J. & PHANIKUMAR, M.S. 2020 Direct numerical simulations of turbulence and hyporheic mixing near sediment–water interfaces. *J. Fluid Mech.* **892**, A20.

STOYANOVA, P.V., WANG, L., SEKIMOTO, A., OKANO, Y. & TAKAGI, Y. 2019 Effect of thin and rough layers of porous materials on drag. *J. Chem. Engng Japan* **52** (6), 493–500.

SUGA, K. 2016 Understanding and modelling turbulence over and inside porous media. *Flow Turbul. Combust.* **96**, 717–756.

SUGA, K., KUWATA, Y., TAKASHIMA, K. & CHIKASUE, R. 2015 A D3Q27 multiple-relaxation-time lattice Boltzmann method for turbulent flows. *Comput. Maths Applics.* **69** (6), 518–529.

SUGA, K., MATSUMURA, Y., ASHITAKA, Y., TOMINAGA, S. & KANEDA, M. 2010 Effects of wall permeability on turbulence. *Intl J. Heat Fluid Flow* **31**, 974–984.

SUGA, K., MORI, M. & KANEDA, M. 2011 Vortex structure of turbulence over permeable walls. *Intl J. Heat Fluid Flow* **32**, 586–595.

SUGA, K., NAKAGAWA, Y. & KANEDA, M. 2017 Spanwise turbulence structure over permeable walls. *J. Fluid Mech.* **822**, 186–201.

SUGA, K., TOMINAGA, S., MORI, M. & KANEDA, M. 2013 Turbulence characteristics in flows over solid and porous square ribs mounted on porous walls. *Flow Turbul. Combust.* **91**, 19–40.

TANI, I. 1987 Turbulent boundary layer development over rough surfaces. In *Perspectives in Turbulence Studies* (ed. H.U. Meier & P. Bradshaw), pp. 233–249. Springer.

THOMSON, W. 1887 On the division of space with minimum partitional area. *Phil. Mag.* **24** (151), 503–514.

VOERMANS, J.J., GHISALBERTI, M. & IVEY, G.N. 2017 The variation of flow and turbulence across the sediment–water interface. *J. Fluid Mech.* **824**, 413–437.

WANG, L., WANG, W.-W., CAI, Y., LIU, D. & ZHAO, F.-Y. 2020 Effects of porous fins on mixed convection and heat transfer mechanics in lid-driven cavities: full numerical modeling and parametric simulations. *Transp. Porous Med.* **132**, 495–534.

WEAIRE, D. & PHELAN, R. 1994 The structure of monodisperse foam. *Phil. Mag. Lett.* **70**, 345–350.

WHITAKER, S. 1996 The Forchheimer equation: a theoretical development. *Transp. Porous Med.* **25**, 27–61.

WHITE, B.L. & NEPF, H.M. 2007 Shear instability and coherent structures in shallow flow adjacent to a porous layer. *J. Fluid Mech.* **593**, 1–32.

XU, H.H.A., ALTLAND, S.J., YANG, X.I.A. & KUNZ, R.F. 2021 Flow over closely packed cubical roughness. *J. Fluid Mech.* **920**, A37.

ZIPPE, H.J. & GRAF, W.H. 1983 Turbulent boundary-layer flow over permeable and non-permeable rough surfaces. *J. Hydraul. Res.* **21**, 51–65.